Constraining global carbon budget using vertically-integrated CO_2 measurements

Thesis by

Zhonghua Yang

In Partial Fulfillment of the Requirements

for the Degree of

Doctor of Philosophy

California Institute of Technology

Pasadena, California

2007

(Submitted 13th December 2007)

To My Family

Acknowledgments

Most importantly, I must thank my advisors Paul Wennberg (California Institute of Technology) and Jim Randerson (University of California at Irvine). I am always inspired by Paul's clear vison of science and Jim's passion for research work. Their warm supports and advices have made me feel at home, even in a foreign country on the other side of the Earth.

I am grateful to other faculty members and scientists at Caltech's Division of Geological and Planetary Sciences and Jet Propulsion Laboratory, particularly Jess Adkins, Geoffrey Toon, Tapio Schneider, Stanley Sander, Yuk Yung, Andrew Ingersoll, Richard Cageao, and Linda Brown, for mentoring me and involving me in research. Seth Olsen, Ross Salawitch, Jean-Francois Blavier, Jack Margolis, and Norten Allen (at Harvard) have given me valuable guidances in my graduate career, especially on the perennial fighting against computer problems.

Life at Caltech has been a wonderful experience. Rebecca Washenfelder, Gretchen-Keppel Alex, and Nir Krakauer have been great friends and collaborators. Friendship from Tingwei Mu (Chemistry), Justin Bois (Chemical Engineering), Kai Shen (Neuroscience), and Huiyu Li (Geochemistry) have also greatly helped me in life beyond research. I also have really enjoyed my time in both Wennberg and Randerson group, with Rebecca Washenfelder, Gretchen-Keppel Alex, Alan Kwan, Julie Fry, John Crounse, Karena McKinney, Coleen Roehl, Yael Yavin, David McCabe, Kathleen Spencer, Lisa Welp, Nicole Smith Downey, Nir Krakauer, Jamie Lindfors, Seth Olsen, Julianna Fessenden, and Heping Liu.

Abstract

I demonstrate that high precision measurements of the vertical-average dry volumn-mixing-ratio of atmospheric carbon dioxide (CO_2) can be obtained from ground-based solar spectra. Oxygen measurements from the same spectra can be used to calibrate CO_2 retrievals across different instruments, enabling a global network of column CO_2 observations to be constructed. I also illustrate that this new type of data, together with aircraft profile CO_2 observations, provide new constraints on global carbon fluxes.

Contents

List of Figures

List of Tables

Chapter 1

Introduction

1.1 Global warming and the carbon budget

Global warming is one of the biggest challenges facing mankind in our time [*Dickinson and Cicerone*, 1986], with various predictions of its disastrous consequences. These predictions include: rise of sea-level [*Meehl et al.*, 2005], increase of extreme weather events [*Emanuel*, 1987; *Knutson and Tuleya*, 2004], and altering of agriculture pattern [*Adams et al.*, 1990; *Mendelsohn et al.*, 1994; *Rosenberg*, 1981]. While some of the consequences are already observable [*Levitus et al.*, 2000; *Goldenberg et al.*, 2001; *Emanuel*, 2005; *Webster et al.*, 2005], the warming is on-going and continuously driven by emissions of "greenhouse gases" (e.g. CO_2, CH_4, and CFCs[1]) as byproducts of human activities. These gases increase the absorption of long wavelength radiative energy from the Earth surface and warm the climate. The key to controlling global warming, therefore, lies in our ability to control the emission of such gases [*HaDuong et al.*, 1997; *Corfee-Morlot and Hohne*, 2003; *Kallbekken and Rive*, 2007].

Since the most important greenhouse gases are compounds of carbon (water vapor excluded), understanding the carbon sources and sinks at global scale (i.e. the global carbon budget) is a prerequisite for a global warming control strategy. Numerous studies during the last five decades

[1] or chlorofluorocarbons

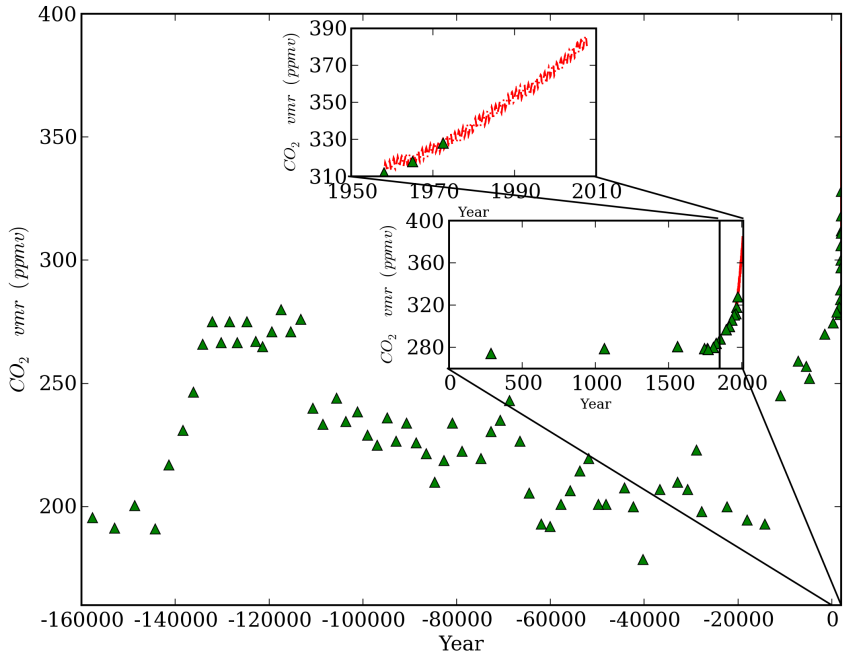

Figure 1.1: The atmospheric CO_2 concentration since 160,000 years ago. The fast increase of CO_2 concentration after 1850 is highlighted. The green triangles are palieclimate measurements of CO_2 contents in the Vostok ice core [*Barnola et al.*, 1987; *Neftel et al.*, 1985], and the red line shows the air sample of Mauna Loa observatory after 1958 [*Tans*, 2007b].

(e.g. [*Keeling*, 1958, 1961; *Takahashi*, 1961; *Houghton et al.*, 1983; *Eamus and Jarvis*, 1989; *Jarvis*, 1989; *Keeling and Shertz*, 1992; *Tans et al.*, 1993; *Keeling et al.*, 1996]) have constructed a picture of the carbon budget, that include all transportation and transformation processes of different forms of carbon compounds taking place on the Earth (Figure 1.3). Some important discoveries related to atmosphere carbon contents are:

- The atmosphere carbon dioxide level fluctuated from 180 to 300 ppmv (parts per million by volume) in the past 420,000 years [*Barnola et al.*, 1987] and stayed around 280 ppmv for several millanium until around 1750 [*Neftel et al.*, 1985], when the industrial revolution took off. Since then, anthropogenic carbon sources have rapidly driven the atmosphere CO_2 to levels unprecedented in past 100,000 years – 315 ppmv in 1958 and 379 ppmv in 2005 (Figure 1.1)[*IPCC*, 2007].

- Fossil fuel combustion and cement production are the primary anthropogenic carbon sources into the atmosphere, contributing to about 2/3rds of the total anthropogenic carbon emission since 1750. The magnitude of fossil fuel fluxes have been growing since the beginning of industrial age [*Andres et al.*, 1996, 1999]. In the first decade of 21^{st} century, the magnitude of this flux is about 6 petagram (10^{15}g or Pg) carbon per year [*IPCC*, 2007; *Marland et al.*, 2007].

- Effect of land use change, notably deforestation, has contributed to another 1/3rd of the cumulative anthropogenic carbon emission after 1750 [*Schlesinger*, 1984; *McGuire et al.*, 2001]. In the 1990s, the emission of carbon from global land use change is around 1.5 Pg/yr [*Dixon et al.*, 1994].

- In recent decades, only about half of the anthropogenic carbon stays in the atmosphere [*Keeling et al.*, 1995], as show in Figure 1.2. The other half, or about 3 PgC/yr, is absorbed by land biosphere and ocean water [*Keeling et al.*, 1996].

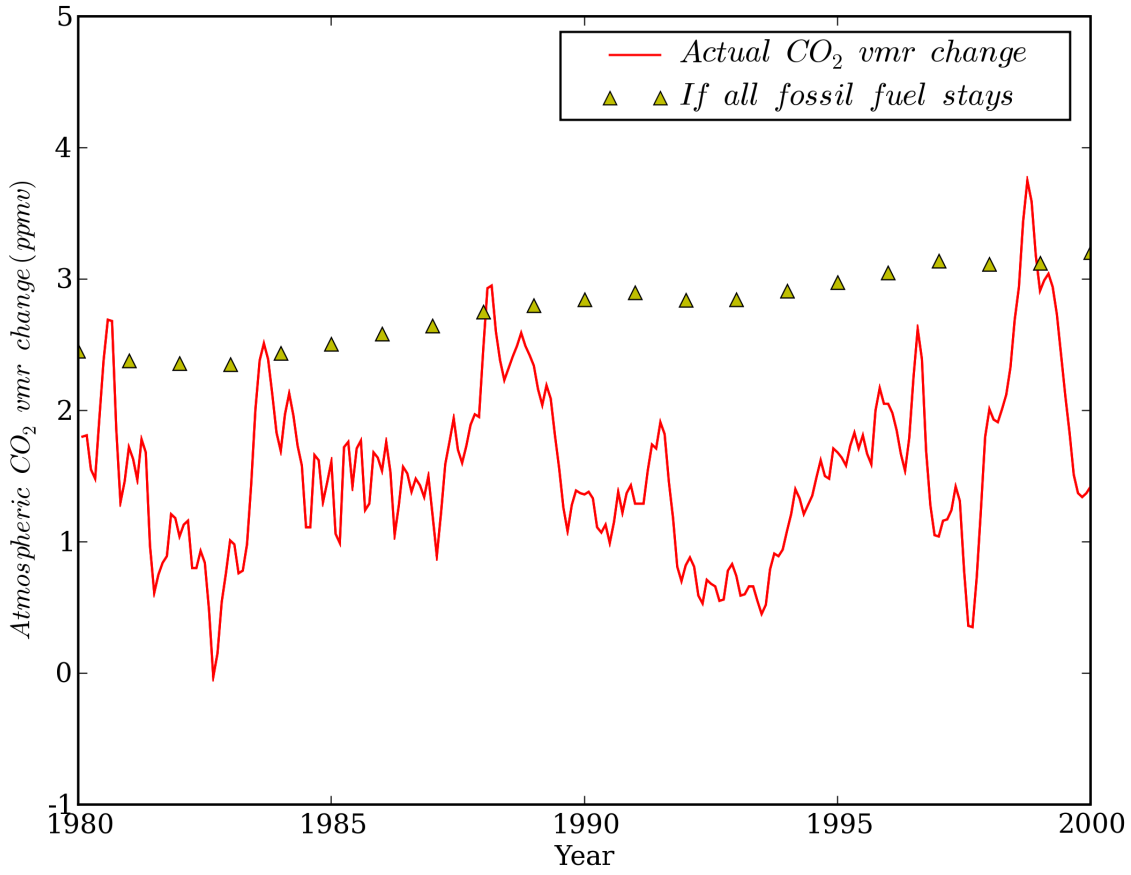

Figure 1.2: The expected atmospheric CO_2 concentration change in ppmv during one year if all fossil fuel emission stays in the atmosphere (yellow triangles, data from *Marland et al.* [2007]), compared with the actual observation (red lines, data from *Tans* [2007b, Online Database]).

The social response to these findings have not produced any significant controls on CO_2 emissions — unlike the success in the control of CFC emission. The Intergovernmental Panel on Climate Change (IPCC) has, however, led the public and policy makers to start discussing possible means of limiting the anthropogenic CO_2 emissions [*Wara*, 2007].

This thesis describes effort on one aspect of the CO_2 control strategy: How to construct a new type of global atmosphere CO_2 observation network — the solar spectral derived column averaged dry air CO_2 mole fraction (X_{CO_2}) observations. This new technology is shown to have high accuracy (~0.2%), and can be used to both validate the future space-borne CO_2 measurements and provide new insights to the global carbon cycle. Its extension to global X_{CO_2}monitoring from space may provide a means of auditing any future carbon control agreement.

1.2 Current measurements of atmosphere related carbon fluxes

By definition, any *conservative* material flux can be expressed as the material inventory change during unit time period:

$$\overline{m} = \frac{m_2 - m_1}{t_2 - t_1} = \frac{\Delta m}{\Delta t} \tag{1.1}$$

Otherwise, the mean flux can also be expressed as the integration of mass flow rate $\vec{m}$ during given time span. Since $\vec{m}$ is determined by flow density ρ and speed $\vec{V}$, plus constant K, we get:

$$\vec{m} = K \cdot \rho \cdot \vec{V} \tag{1.2}$$

$$\overline{m} = \frac{\int_{t_1}^{t_2} \vec{m} \cdot dt}{t_2 - t_1} = \frac{\int_{t_1}^{t_2} K \cdot \rho \cdot \vec{V}}{\Delta t} \tag{1.3}$$

From the definitions above, we can divide various carbon fluxes measurement methods into two groups:

1. Methods that measure the carbon inventory change in a given time period, then derive the mean fluxes;

   (a) Carbon fluxes from fossil fuel and cement production can be derived from documents of energy consumption statistics [*Andres et al.*, 1996, 1999]. The accuracy of these statistics can be quite different in developed and developing countries, but in general they can provide high spatial and temporal resolution (e.g. the fuel consumption of a local power plant can be traced during each hour);

   (b) Fossil fuel carbon amount change can also be derived from other atmosphere species, if the relationship between the species and CO_2 is known. For example, using local biosphere carbon cycle model, Levin et al. have used observations of atmosphere change of CO and SO_2 [*Levin et al.*, 2003; *Levin and Karstens*, 2007] to estimate the fossil fuel emission rate. Similiar approach can be applied to δ^{13}C and δ^{14}C as well [*Turnbull et al.*, 2006; *Hsueh et al.*, 2007];

   (c) Measure atmospheric CO_2 concentration change, then use atmosphere general circulation model and fossil fuel emission to estimate net carbon fluxes of different regions [*Fan et al.*, 1998; *Gurney et al.*, 2002; *Krakauer et al.*, 2004]. This method, if combined with measurements of O_2 [*Keeling et al.*, 1996; *Bender et al.*, 1996] or δ^{13}C [*Ciais et al.*, 1995a,b] of atmosphere CO_2, can also decompose the total fluxes into ocean part and land biosphere part;

   (d) Field biomass inventory in different sample biomes, combined with biome type distribution estimates, can be used to derived the total carbon flux from land biosphere. The biomass inventory can be derived from different sources, such as rountine national forestry statistics [*Kurz and Apps*, 1999; *Fang et al.*, 2001] or history documents of land use changes [*Houghton et al.*, 1983];

(e) Ocean water ΔC^* content change [*Gruber et al.*, 1996; *Sabine et al.*, 2002], combined with CFCs tracked ocean circulation [*Matear et al.*, 2003; *Matsumoto and Gruber*, 2005], can be used to derive the net carbon flux into the ocean

2. Methods that directly measure the flux or the mass flow rate;

   (a) The net carbon flux between vegetated canopy and the atmosphere can be monitored using eddy covariance method, which simultaneously take high-frequency measurements of wind and CO_2 concentrations from towers above the vegetation [*Baldocchi et al.*, 1988, 1996; *Aubinet*, 2000]. A global observation network (FLUXNET) of over 300 sampling sites, covering different type of biomes in five continents, has been in operation continuously since 2001 [*Baldocchi et al.*, 2001, 2006];

   (b) Ocean-atmosphere carbon exchanges can be derived from wind speed and the surface-water carbon dioxide partial pressure (pCO_2) [*Takahashi et al.*, 2002]. One limiting factor of this approach is the complexity of the gas transfer rate dependence on the wind speed [*Wanninkhof*, 1992; *Wanninkhof and McGillis*, 1999]. For example, change of gas transfer dependence equation can increase the annual global ocean flux by 70% [*Takahashi et al.*, 2002]. The difficulty of providing real-time wind observations over oceans was a problem, but this could be improved by recent space-borne wind observations [*Bentamy et al.*, 2003; *Soloviev et al.*, 2007].

Figure 1.3 summaries estimated annual carbon fluxes for the 1990s. Although anthropogenic carbon emission is the main drive behind rising level of atmospheric CO_2, its size (~6 PgC/yr) is more than an order of magnitude smaller than that of either the land biosphere photosynthesis or its respiration during the same time (both are about 120 PgC/yr). The same applies to the carbon fluxes going in and out of ocean as well. The fact that the net atmospheric CO_2 increase is determined by the small differences of several big fluxes is the major difficulty facing the global carbon cycle research.

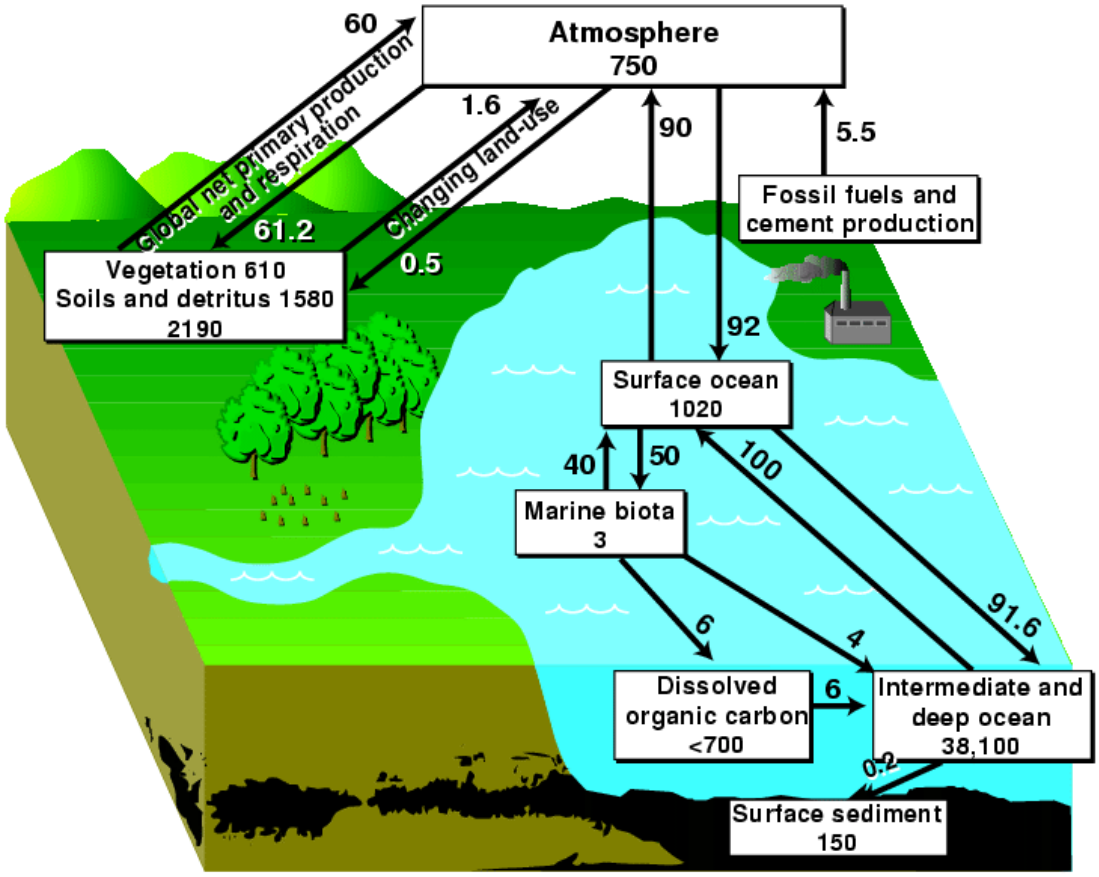

Figure 1.3: The estimated pools and fluxes of global carbon cycle in the late 1990s. All pools are expressed in units of PgC and all annual fluxes in units of PgC/yr. Figure and data are from *IPCC* [1995].

1.3 Spaceborne and ground-based X_{CO_2} observations

To go beyond current methods for estimating global total carbon fluxes, measurements of higher spatial and temporal resolution are required to solve several key problems in carbon cycle research. One such example is the effort to locate the 1~2 PgC/yr "Northern Carbon Sink", which had been speculated to be in either North America [*Fan et al.*, 1998] or Euroasia [*Kauppi et al.*, 1992] by different inversion estimates. It was later shown that the exact location and mechanism of this carbon sink can not be robustly constrained by current surface CO_2 observations [*Gloor et al.*, 2000; *Gurney et al.*, 2002; *Houghton*, 2003]. A recent study using aircraft CO_2 profiles (which provide vertical coverage) find the "Northern Sink" is non-existent and instead locates a "Tropical Carbon Sink" [*Stephens et al.*, 2007], after applying correction for vertical mixing bias in inversion models. However, limited by fewer sampling sites (12 profile vs. ~100 surface) and much lower sampling rate (weekly for profile vs. hourly for surface), the sampling error of CO_2 profiles is much larger than that of surface CO_2 observations, making this study less robust.

Spaceborne CO_2 observations with frequent (e.g. biweekly to monthly) global coverage and high spatial resolution (~ 10^4 km^2) are proposed as the next generation of carbon cycle observation. Future missions of this type include the Orbit Carbon Observatory (OCO) of Jet Propulsion Laboratory [*Crisp et al.*, 2004] and the Greenhouse gases Observing Satellite (GOSAT) of Japan Aerospace Exploration Agency [*Masahiro and Takashi*, 2005]. They have great advantages over the traditional surface CO_2 sampling networks, especially for the purpose of deriving carbon fluxes from regions of continental to sub-continental size [*Rayner and O'Brien*, 2001; *Chevallier et al.*, 2007] (e.g. Northern American Carbon Sink).

Both missions will obtain spectra of surface-reflected sunlight at both CO_2 and O_2 absorption bands in the near IR region. Atmospheric CO_2 concentration will be retrieved from the spectra using molecule absorption cross sections determined in the laboratory. This method measures the mean CO_2 mixing ratio along the photon path of the sun light (or X_{CO_2}). In contrast, the existing CO_2 networks (e.g. GlobalView-CO_2) measure the CO_2 mixing ratio at the sampling point. This

important difference (as shown in [*Olsen and Randerson*, 2004]) means the future data from CO_2 observation satellites can not be readily calibrated by current observations, and a new validation strategy must be developed together with the satellites.

Ground-based solar spectral observations have been used to monitor trace gases in the Earth atmosphere, including ozone [*Pougatchev et al.*, 1995], HDO [*Schneider et al.*, 2006], NO_x and CFCs [*Notholt et al.*, 1995]. As show in Figure 1.4, the ground-based spectral observatories can use the same molecule spectroscopy and much stronger light source directly from the sun. They thus provide an ideal calibration for the spaceborne CO_2 observations. These spectral observations also have another big advantage over existing point samples, in that they average through the changes in the atmosphere boundary layer height and are much less sensitive to these noises.

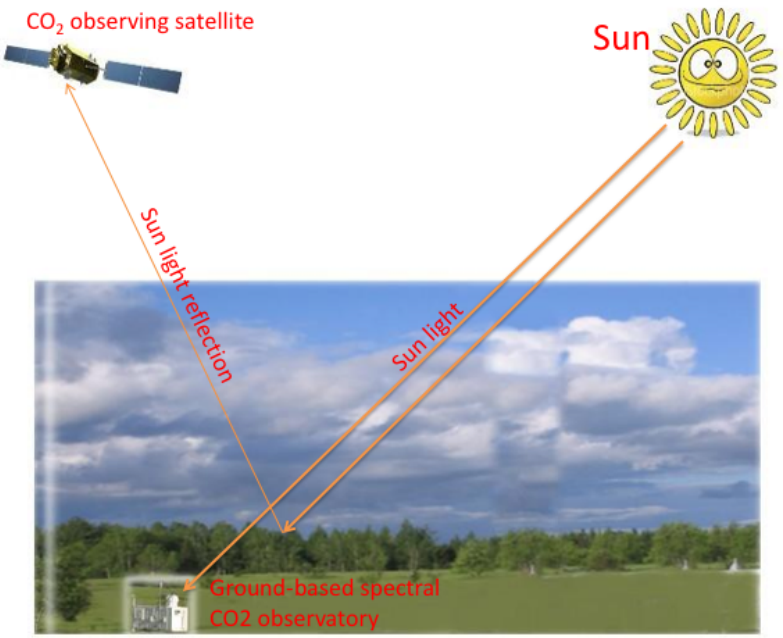

Figure 1.4: CO_2 observing satellite and ground-based spectral observatory

1.4 Outline of the Dissertation

This work explores three issues related to ground-based spectral CO_2 measurements: 1) the technical achievable precision for a single instrument; 2) the method to inter-calibrate observations from different instruments and different sites; and 3) the advantage of using this type of observations to constrain global carbon budget.

Chapter 2 presents our retrieval of X_{CO_2} from existing high-resolution solar absorption spectra obtained during period 1977-1995 at Kitt Peak National Observatory. The spectra cover both the CO_2 band at 6300 cm^{-1} and the O_2 band at 7900 cm^{-1}. The CO_2 and O_2 amount were first derived separately based on lab spectroscopy, and then ratioed to give the X_{CO_2}. The precision of this technique is better than 0.5%, and has since been greatly improved in our new project by employing specifically designed instruments [*Washenfelder et al.*, 2006].

Chapter 3 demonstrates the possibility of using retrieved atmospheric oxygen column mixing ratio to calibrate a ground-based spectral CO_2 observation network. To improve precision, we took new solar absorption spectra from Table Mountain Facility in 2003, with special attention on observation timing. These spectra were then analyzed at 13160 cm^{-1} to yield the oxygen column mixing ratio, which is in turn compared with the photon paths based on geometrically ray-tracing calculation. The comparison shows that the oxygen spectral retrievals can provide a precision of about 0.2%, which indicates oxygen can serve as the benchmark for inter-calibration among different instruments and observation sites of a network.

Chapter 4 describes our first effort to use column X_{CO_2} to constrain the global carbon budget. In this work, we analyzed several column CO_2 datasets, including new measurements from the first observatory of Total Carbon Column Observing Network (TCCON). We find these observations indicate a significantly larger (>25%) net ecosystem exchange in the Northern Hemisphere than current biosphere model prediction. We also used aircraft CO_2 profile data to illustrate that these underestimates may come from too weak vertical mixing in atmosphere transport models.

The last chapter includes a summary of the future methods proposed to observe the global carbon budget, and a short discussion on the improvement they will contribute to the big picture: Improving our understanding of the exchange of CO_2 between the land, ocean, and atmosphere.

Chapter 2

Atmosphere CO_2 column mixing ratio over Kitt Peak from 1979 to 1995 [1]

Abstract

The column-averaged volume mixing ratio (VMR) of CO_2 over Kitt Peak Arizona was retrieved from high-resolution solar absorption spectra obtained with the Fourier transform spectrometer on the McMath telescope. Simultaneous column measurements of CO_2 at ~6300 cm^{-1} and O_2 at ~7900 cm^{-1} were ratioed to minimize systematic errors. These column ratios were then scaled by the mean O_2 VMR (0.2095) to yield column-averaged VMRs of CO_2, which display similar behavior to the Mauna Loa in situ surface measurements. During the period 1977-1995, the column-averaged mixing ratio of CO_2 increased at an average rate of 1.49 $\pm$ 0.04 ppmv/yr with seasonal variations of ~7 ppmv peak-to-peak. Our retrievals show that this remote technique is capable of precisions better than 0.5%, and can be greatly improved by employing specifically designed instruments.

[1] Adapted from Z. Yang, G. C. Toon, J. S. Margolis, P. O. Wennberg (2002), Atmospheric CO_2 retrieved from ground-based near IR solar spectra, *Geophysical Research Letters*, 29(9), 1339, doi: 10.1029/2001GL014537

2.1 Introduction

The atmospheric CO_2 VMR has increased from about 280 ppmv in pre-industrial times (before 1800) to about 360 ppmv by the 1990s. Previous studies based on observations from the *in situ* network of surface stations indicate that the biosphere and ocean sinks are absorbing about half of the anthropogenic CO_2 emission [*Battle et al.,* 2000]. The nature and geographic distribution of these sinks, however, remains too uncertain to predict their responses to future climate or land use changes [*IPCC,* 2001]. Although *in situ* measurements of CO_2 from the existing surface network are highly accurate (0.1 ppmv), their sparse spatial coverage (both vertical and horizontal) limits their usefulness in constraining models of CO_2 sources and sinks.

Rayner and O'Brien [2001] have shown that global satellite measurements of the CO_2 column, even with poorer precision (2 ppmv, 0.5%), would provide a better constraint on geographic and temporal distribution of CO_2 sources and sinks than the existing surface network. This calculation assumes, however, that such space-borne observations are bias-free. To test and eliminate bias, an extensive correlative measurement effort will be required. These measurements, additionally, can be important for constraining aspects of the CO_2 behavior that will not be measurable from space in the foreseeable future (e.g. diurnal variations). *In situ* measurements of CO_2 from the existing surface network *cannot* alone be used to validate space-borne measurements of column CO_2 due to their much higher spatial resolution and their confinement to the planetary boundary layer.

Ground-based spectral observations of the sun at high spectral resolution can, in principle, be used to determine the total CO_2 column. The near IR is particularly attractive for this task because the sun is sufficiently bright that high signal-to-noise (S/N) with high spectral resolution can be obtained during minimal integration time.

2.2 Measurements

Between 1979 and 1985, numerous high-resolution absorption spectra ($\Delta v = 0.014$ cm^{-1}) of the Sun were obtained with the 1-m Fourier Transform Spectrometer (FTS) at the McMath telescope complex on Kitt Peak (31.9°N, 111.6°W, 2.07 km above sea level). Observations covering the spectral range from 6000–8000 cm^{-1} were used to determine the column-averaged dry air VMR of CO_2 and CH_4 [*Wallace and Livingston*, 1990]. In that work, equivalent width analyses (EQW) were performed on 19 well isolated lines of the CO_2 (21°2)-(00°0) band ($v_0 = 6348$ cm^{-1}) and 14 lines of the O_2 0-0 $^1\Delta_g - ^3\Sigma_g^-$ band ($v_0 = 7882$ cm^{-1}) to get the column amount of both gases. Assuming the O_2 VMR to be constant (0.20946), the column ratio (CO_2/O_2) was scaled to yield the column-averaged CO_2 VMR in the atmosphere over Kitt Peak.

In this letter, we report a reanalysis of the Kitt Peak observations using a more sophisticated spectral retrieval algorithm with updated spectroscopic linelists for CO_2, O_2 (including the collision induced absorption), H_2O, and absorption in the solar atmosphere. In our analysis, we simultaneously fit all lines (more than 200) in the entire O_2 band and two CO_2 bands centered at 6228 cm^{-1} and 6348 cm^{-1}. This allows us to include in our analysis spectra obtained at high airmasses, that *Wallace and Livingston* [1990] excluded due to limitations imposed by the EQW technique. In addition, we have analyzed spectra obtained more recently at the same facility.

2.3 Data analysis

Spectra are analyzed using a line-by-line algorithm developed at Jet Propulsion Laboratory for the analysis of solar absorption spectra. In the retrieval, least square analysis is performed over a prescribed spectral window to derive the *slant column abundance* of the target gases. The fitting

residual is defined as:

$$\chi^2 = \sum \frac{(Y_i^M - Y_i^C(x))^2}{\sigma_i^2} \tag{2.1}$$

In which $Y_i^M$is one measurement in one spectrum, Y_i^C is the forward model calculation, x is the target gas scale factor, σ_i is the uncertainty of Y_i^M. In our forward model the atmosphere is represented by 70 vertical levels. Pressure- and temperature-dependent absorption coefficients are computed line-by-line for each level and used in the forward model to produce spectra $Y_i^C(x)$ for comparison.

Pressure and temperature profiles are obtained from NOAA's Climate Diagnostics Center (CDC), which are assimilated temperature data on 17 levels from 1000 to 10 mbar with $1^\circ \times 1^\circ$ geographic resolution. For levels with pressure smaller than 10 mbar, climatological temperature profiles are used. A study of the temperature sensitivity of the retrieved CO_2/O_2 ratio revealed a T-dependence of 0.07%/K. So if the CDC profiles were systematically in error by 5 K at all levels, the CO_2/O_2 error would be 0.35% or about 1 ppmv.

The CO_2 spectral parameters are derived from the latest *high-resolution transmission molecular absorption database* (HITRAN) [*Rothman et al.*, 1998]. The background solar linelist is based on the work of *Wallace and Livingston* [1990]. For the O_2 lines, the HITRAN strengths were updated with a recent recalculation [*Goldman*, private communication] that was found to give improved agreement with laboratory data [*Newman et al.*, 2000]. In addition to the discrete O_2 lines of the $^1\Delta$ band, there is also underlying O_2 continuum absorption [*Smith and Newnham*, 2000; *Smith et al.*, 2001]. Although this O_2 collision induced absorption (CIA) was included in the line-by-line calculation to improve estimation of the continuum, only the discrete $^1\Delta O_2$ lines were used in the computation of the O_2 column amount.

2.4 Results

414 spectra obtained at Kitt Peak over the period 1977-1995 have been analyzed. Due to other demands on the instrument, solar observations in the 6000 – 8000 cm^{-1} spectral region were generally made on only a few days each year. The spectra were measured at various times throughout the day from sunrise to sunset, weather permitting. The spectra analyzed are generally co-additions of 2-4 individual spectra, each taking 7 minutes to acquire. The effective solar zenith angle (SZA) was calculated as the average of the SZAs of the individual interferograms at their *zero path difference* (ZPD) times. At high airmasses (~10), this was often significantly different (5% in airmass) from the mean SZA, due to the fact that the ZPDs were typically not in the middle of the double-sided interferograms, and due to the non-linear nature of the variation of the airmass with time.

Examples of the spectral analysis are shown in Figure 2.1. Two spectral windows for CO_2 and one window for O_2 were employed as shown. Since most of these spectra were not intended for use in the 6000 – 8000cm^{-1} region, we have excluded 71 observations (17% of the total) that produce rms spectral residuals greater than 6.0% for O_2 or 3.0% for CO_2. The larger threshold for rejection of O2 spectra is due to the difficulty in fitting the O_2 CIA at large SZAs. In remaining spectra, those measured at low SZA generally have rms residuals of about 0.4-0.8% for O_2 and 0.7-0.8% for the CO_2. These residuals are dominated by solar features and by the O_2/CO_2 lines themselves. For spectra measured at high SZA (>75°) the residuals are larger (up to 3% in CO_2 and 5% in O_2) due to the increasing strengths of the O_2/CO_2 lines.

The retrieved slant column amounts were divided by the calculated airmass to produce vertical column amounts. Account was taken of the 250 m optical path inside the telescope, which adds nearly 3% to the noontime O_2 slant column. The daily-average value of CO_2 and O_2 vertical column amounts and their ratio (CO_2/O_2) are shown in Figure 2.2. The long-term trend in the CO_2 column amounts (Panel A) is evident, but the seasonal variation is unclear. For the O_2 column amount (Panel B), no long-term trend is observed. The retrieved dry VMRs (converted from column amount after dividing by 2.15×10^{21} times the surface pressure in mbar) of O_2 fall within the

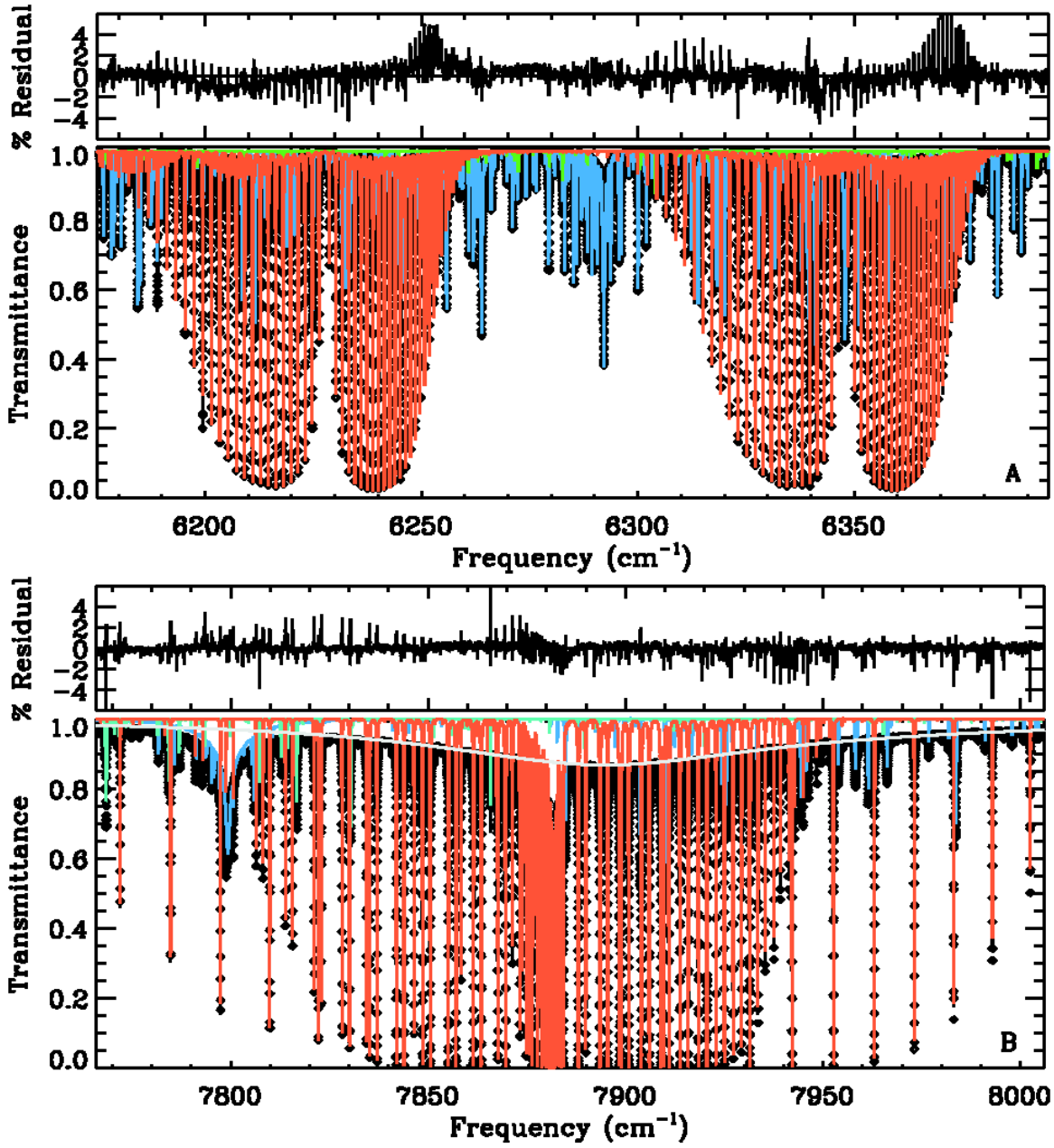

Figure 2.1: The spectrum was measured at 70.70°SZA on May 9, 1981. Diamonds are the measurements and black lines are the fitted transmittance. (a) The 6100 – 6400 cm^{-1} region, containing the (14°1)-(00°0) and (21°2)-(00°0) bands of CO_2; (b) The 7800 – 8000 cm^{-1} region, containing the O_2 0-0 $^1\Delta_g - ^3\Sigma_g^-$ band. The contributions from CO_2/O_2, H_2O and solar features are shown by the red, green and blue lines respectively. The O_2 CIA is represented by the grey line in (b). The residual traces (measured-calculated) and are clearly dominated by systematic errors in both regions.

range of 0.202 to 0.217, with a mean of about 0.209 – remarkably close to the actual O_2 VMR for dry air (0.2095).

The ratio of the CO_2 and O_2 column amounts, scaled by the standard atmospheric O_2 fraction of 0.2095, gives the column-averaged dry volume-mixing ratio of CO_2 in the atmosphere (Figure 2.2, Panel C). Clearly, the precision of the CO_2/O_2 ratio is improved over that of the CO_2 column. The high degree of correlation between errors in CO_2 and O_2 suggests that much of the scatter in the unratioed observations is common to both spectral regions. We speculate that these errors arise in the spectra (e.g. uncertainties in instrumental line shape) or in the calculated airmass (e.g. uncertainty in surface pressure or SZA). In Figure 2.2, we have scaled the CO_2 column average dry mixing ratio by 1.058. This scaling was empirically determined to minimize bias between the Kitt Peak data and those from Mauna Loa, and probably reflects an error in the CO_2 line strengths and/or pressure broadening coefficients. Also shown in Figure 2.2(Panel C) are the Mauna Loa CO_2 *in situ* measurements. Their trend and seasonal cycle are remarkably similar to the Kitt Peak data. The average CO_2 increase between 1977 and 1995 is 1.49 ± 0.04 ppmv/yr, the same as that measured from Mauna Loa (~1.47 ppmv/yr) over the same period.

Details of the seasonal cycles for CO_2/O_2 in the period 1979-1985 are expanded in Figure 2.3. We compared the Kitt Peak data with two sets of *in situ* measurements: Mauna Loa (19.5°N, 155.6°W, 3397 m above sea level) and Niwot Ridge (40.1°N, 105.6°W, 3475 m above sea level). The phase of Kitt Peak data is nearly the same as Mauna Loa measurements but has a lag of about one month compared with the Niwot Ridge record, despite the latter site being much closer to Kitt Peak. The seasonal amplitude of Kitt Peak data (~7 ppmv peak-to-peak) is also more similar to Mauna Loa record than to the Niwot Ridge record. We do not know the reason for the different behavior of the Niwot Ridge data, but we speculate that the Mauna Loa and Kitt Peak records might better represent the free tropospheric CO_2, while the Niwot Ridge record is more heavily influenced by local sources and sinks of CO_2.

To understand the diurnal variation and to estimate the precision of the retrieval, 231 column results

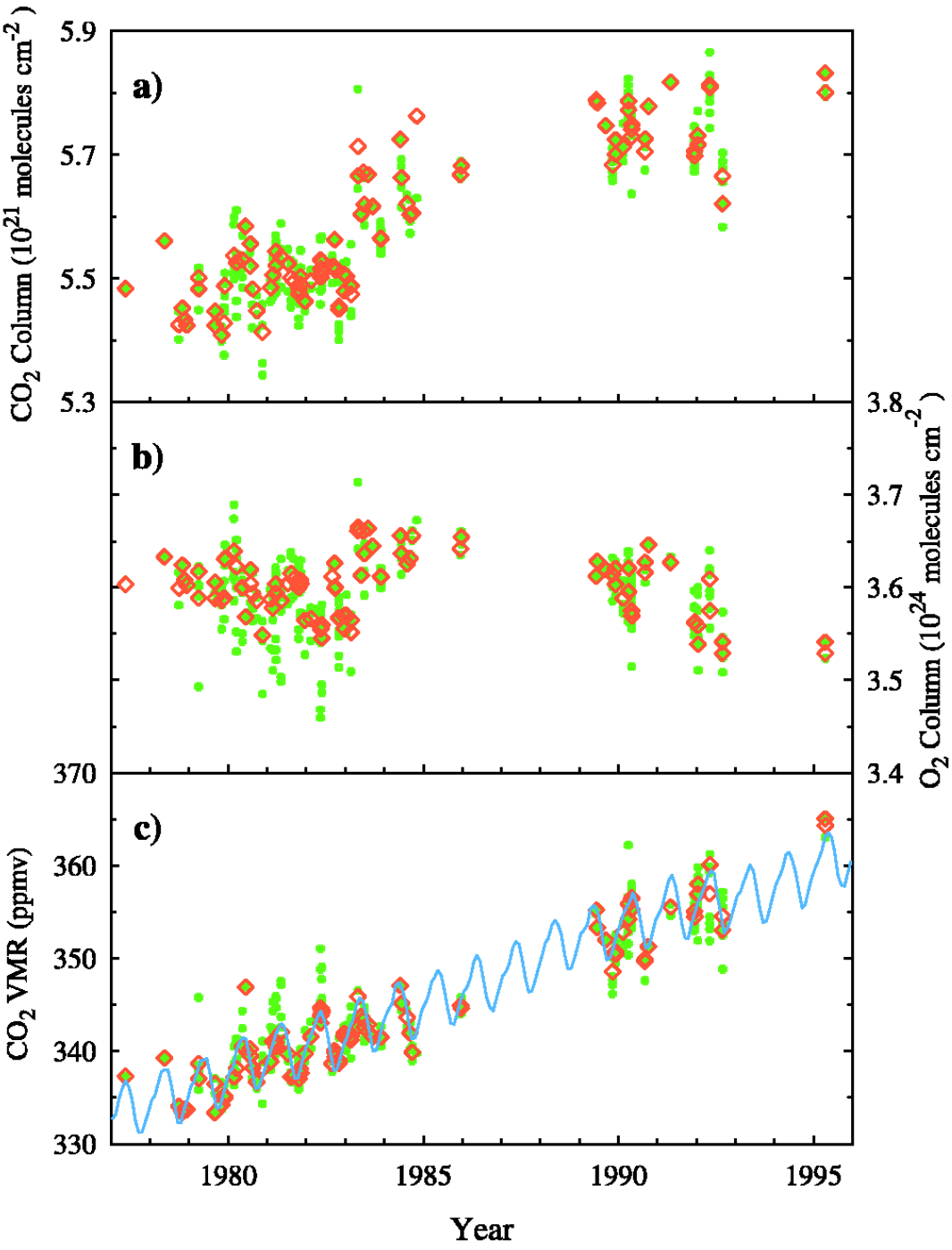

Figure 2.2: (a) CO_2 and (b) O_2. (c) the column-averaged CO_2 VMR over Kitt Peak determined from the ratio of the individual CO_2 and O_2 spectra (green dots) and the daily-averaged value (red diamonds) are shown. The column measurements have been scaled by 1.058 to match the absolute value of the Mauna Loa record (blue). Error in the spectroscopic database for CO_2 is likely responsible for the discrepancy (see text).

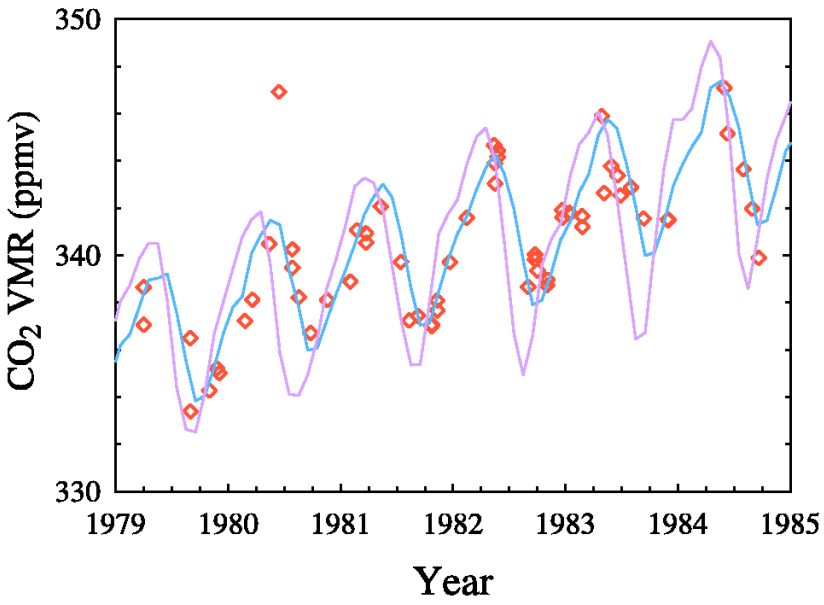

Figure 2.3: Time series of daily averaged retrieved values of the Kitt Peak column CO_2 VMRs (red open diamonds) over period 1979-1985, compared with the Mauna Loa (blue) and the Niwot Ridge (pink) in situ measurements.

for the 40 different days for which more than 4 column measurements exist were analyzed. For each day, the O_2 and CO_2 vertical column amounts were converted into VMRs and averaged to get the daily mean. The variation of one measurement from the daily mean is defined as

$$Diurnal\ variation\ of\ x = \frac{x}{\overline{x}} - 1 \tag{2.2}$$

where x is one measurement and $\overline{x}$ is the mean of the day. The diurnal variations for O_2 and CO_2 obtained in this manner are partly correlated and therefore the CO_2/O_2 ratios exhibit less error than CO_2 VMRs obtained by dividing the CO_2 column amount by pressure. The range for O_2 variation is 2.0%, whereas for CO_2 it is 1.2%.

The diurnal variations in the CO_2/O_2 ratios are shown in Figure 2.4. Most of the deviation is in the range of -0.5~0.5%, except for a few measurements made at high airmasses (>10). Assuming the CO_2 VMR over Kitt Peak is essentially constant during one day, the scatter in Figure 2.4 is a

measure of the precision of the column measurements. The origin of the increase of CO_2/O_2 at high airmass is likely non-geophysical. We speculate that the different behaviors of the continuum signal in the CO_2 and O_2 spectral regions as a function of airmass contributes to this anomalous diurnal behavior in CO_2/O_2. Since the integrating periods of the Kitt Peak measurements are quite long (about 30 minutes at 5 airmasses and 15 minutes at 10 airmasses), it is impossible to un-ambiguously assign an average airmass to these spectra.

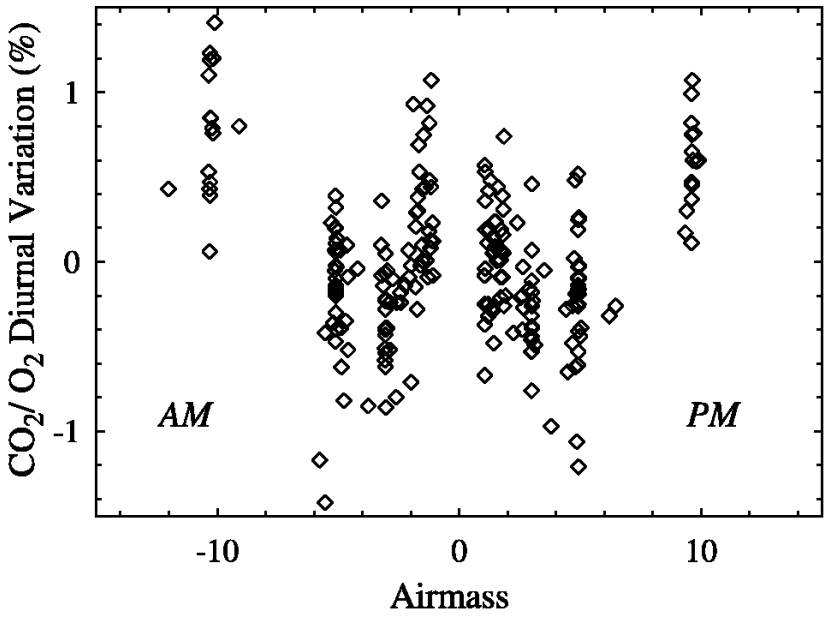

Figure 2.4: Diurnal variations of the CO_2/O_2 ratio (see page 22 for detail)

2.5 Conclusions

Reanalysis of near IR spectra obtained at Kitt Peak National Solar Observatory have demonstrated that the column-averaged CO_2 VMR can be retrieved with ~0.5% precision. By simultaneously fitting all lines in one band and using new spectroscopic linelists, we decreased the temperature sensitivity of data retrieval and greatly improved the precision compared with Wallace and Livingston's analysis.

We believe that remaining errors are dominated by deficiencies in the spectroscopic linelists, and by airmass ambiguities exacerbated by the long scan duration of the Kitt Peak spectrometer. With improvements to the spectroscopic linelists and with modern, faster-scanning FTIR spectrometers dedicated to the measurement of CO_2, substantially better results can be anticipated. We are confident that with these improvements, this technique will be more than adequate for ground-truthing future space-based CO_2 column observations.

Chapter 3

Ground-based photon path measurements from solar absorption spectra of the O_2 A-band[1]

Abstract

High resolution solar absorption spectra obtained from Table Mountain Facility (TMF, 34.38°N, 117.68°W, 2286 m elevation) have been analyzed in the region of the O_2 A-band. The photon paths of direct sunlight in clear sky cases are retrieved from the O_2 absorption lines and compared with ray-tracing calculations based on the solar zenith angle and surface pressure. At a given zenith angle, the ratios of retrieved to geometrically derived photon paths are highly precise (~0.2%), but they vary as the zenith angle changes. This is because current models of the spectral lineshape in this band do not properly account for the significant absorption that exists far from the centers of saturated lines. For example, use of a Voigt function results in an error in the retrieved photon path of as much as 5%, highly correlated with solar zenith angle. Adopting a super-Lorentz function reduces, but does not completely eliminate this problem. New lab measurements of the lineshape are required to make further progress.

[1]Adapted from Z. Yang, P. O. Wennberg, R. P. Cageao, T. J. Pongetti, G. C. Toon, S. P. Sander (2005), Ground-based photon path measurements from solar absorption spectra of the O_2 A-band, *J. Quant. Spectrosc. Radiat. Transfer*, 90, 309-321

3.1 Introduction

The A-band is the strongest absorption band of O_2 in the visible and IR region. Its importance for atmospheric remote sensing lies not in measuring O_2 itself (the mixing ratio is well known), but rather in its use of determining the photon paths traversed through the atmosphere. Because the A-band has the virtue of being in a window region (where atmosphere is transparent down to the surface) and free from interference of other atmospheric gases (e.g. water vapor), transmission and reflectance spectra of this band are sensitive to ray path changes in the troposphere and thus directly relevant to the study of clouds and aerosols from space [*Yamamoto and Wark*, 1961; *O'Brien and Mitchell*, 1992; *Kuze and Chance*, 1994; *Asano et al.*, 1995; *Min et al.*, 2001]. The A-band spectra have also been used for estimating surface pressure from aircraft [*O'Brien et al.*, 1998] and deriving tangent heights for solar occultation observations .

Photon path information is extremely important for achieving the required precision of future global-coverage space-borne measurements of CO_2, which are necessary for resolving the global carbon budget. Similar applications on other well-mixed gases (e.g. CH_4) are possible. These measurements must have very high precision (e.g. 1 ppmv or 0.3% for CO_2) to detect small geographic and temporary changes. The usefulness of the O_2 A-band in improving space-borne CO_2 measurements, however, is predicated on accurate simulation of its absorption spectrum [*Kuang et al.*, 2002].

Retrieval of photon path lengths with sub-percentage precision from atmospheric spectra is always a challenge. For the A-band, the high optical depths mean that most of the lines are saturated from the centers to ~10 Lorentzian widths, even at the smallest airmass (the ratio of the slant column to the vertical column). The information on the photon paths, therefore, comes largely from the far-wings of these O_2 absorption lines where existing laboratory constraints are inadequate. Retrievals from highly saturated spectra also require precise knowledge of both the continuum and zero levels. In addition, accurate temperature information is needed. Finally, the absorption lines in this band

are strongly overlapped (especially for lines in the R branch), and line-mixing effects could be important.

In this paper, we evaluate the accuracy of photon path retrievals from the A-band spectra in a situation where the photon paths are very well known: ground-based narrow field-of-view observation of direct sunlight in near-IR region. In this observation geometry, virtually all the measured photons have passed through the atmosphere without being scattered. The photon paths can, therefore, be accurately determined by simple geometric ray tracing. The main purpose is to develop an algorithm and technique that will allow retrieval of photon path information from the ground-based A-band spectra, and to explore the accuracy-limiting factors.

3.2 Measurements

The data analyzed in this work were obtained with the Fourier Transform Ultraviolet Spectrometer (FTUVS), installed at JPL's Table Mountain Facility, about 40 miles Northeast of Los Angeles [*Cageao et al.*, 2001]. The instrument is designed specifically for use in the visible and near-UV, but is able to work in the near-IR as well using a Silicon photodiode detector. Measurements were taken on 12 days between March 24 and April 11, 2003, each consisting of 10 scans (5 forward and 5 reverse) obtained in 5 minutes. The forward and reverse scans were summed separately in order to evaluate the systematic error from different scan directions. Altogether 540 spectra were obtained from 10450 to 17987 cm^{-1}, covering the entire A-band (centered at 13120 cm^{-1}), with a resolution of 0.054 cm^{-1}. To minimize the measurement variation, the instrument settings and alignment were adjusted minimally during the 19 days.

We recorded the beginning and ending times of each measurement with an error smaller than five seconds. This translates to photon path accuracies better than 0.06% at two airmasses and 0.17% at five airmasses. The surface pressures were recorded at the same time. We also noted cloudiness and only use spectra taken in clear sky cases.

3.3 Data analysis

Spectra are analyzed using the GFIT algorithm developed at Jet Propulsion Laboratory. This algorithm is able to simultaneously retrieve the column amounts of several molecules from a prescribed spectral window. In the forward model, we represent the atmosphere by 70 levels from 0 to 69 km. Pressure- and temperature-dependent absorption coefficients are computed line-by-line for each level. The atmospheric transmittance T at frequency v_i is represented as

$$T(v_i) = \exp[-\sum p_l n_l \sum \lambda_g m_{l,g} \sum s_{l,g,k} f_{l,g,k}(v_i - v_{l,k})] \tag{3.1}$$

Where p_l and n_l is the *effective optical path length* and the total *atmospheric number density* (molecule cm^{-3}) at the l^{th} level; $m_{l,g}$ is the a priori volume-mixing ratio (VMR) of the g^{th} gas at the l^{th} level; $s_{l,g,k}$ and $f_{l,g,k}$ is the absorption strength (cm molecule^{-1} cm^{-1}) and normalized lineshape function of the k^{th} absorption line of the g^{th} gas at the l^{th} level; and $v_{l,k}$ is the center frequency (cm^{-1}) of the k^{th} absorption line at the l^{th} atmospheric level. λ_g is the scale factor applied to the VMR of the g^{th} gas (for a gas with accurately known mixing ratio such as O_2, λ_g is effectively the photon path scale factor). The pressure and temperature profiles for each day's spectra are rescaled from NCEP/NCAR reanalysis data, which include temperatures on 17 levels from 1000 to 10 mbar with 2.5°×2.5° geographic resolution. Climatological temperature profiles are used for levels with pressure 10 mbar. The optical path length between each level is calculated based on time-derived astronomical solar zenith angle (SZA), pressure altitude (instead of geometrical altitude to reconcile with the P-T profile), and atmospheric refractive index. All these factors, together with the absorption strengths and lineshape functions, are pre-determined and kept the same during the fitting process.

During the retrieval, the algorithm performs least squares analysis over the spectral window to derive the factors that scale the slant column abundances of the target gases. The fitting residual is

defined as:

$$\chi^2 = \sum \frac{(Y_i^M - Y_i^C)^2}{\sigma_i^2} \tag{3.2}$$

$Y_i^M$is one measurement in the spectrum and σ_i is its uncertainty. $Y_i^C$is the corresponding forward model calculation, which is determined by above-atmosphere solar spectrum , spectral window continuum (approximated linearly as $[\alpha + \beta(v_i - v_c)]$, with α and β the continuum level and tilt, and v_c the window center frequency), zero level offset (Z_{off}), instrument lineshape (ILS), frequency shift (δ) and atmospheric transmittance.

$$Y_i^C = Z_{off} + Y_i^S[\alpha + \beta(v_i - v_c)][ILS(v_i, \delta) \otimes T(v_i)] \tag{3.3}$$

$\otimes$ denotes the convolution operation. During retrieval process, both and its derivatives with respect to the variables are computed iteratively to find the combination of unknowns

$$X = [\lambda_1, \lambda_2 ... \lambda_G, \alpha, \beta, \delta, Z_{off}]$$

that minimize the residual χ^2.

Figure 1(a) shows a raw spectrum and the parameters applied to fit it. The upper line represents the linearized continuum level and the lower line represents the Z_{off}. During fitting, the continuum level is determined from regions where the atmospheric absorption is minimal (i.e. beyond the edges of the band), and the Z_{off} is determined from blacked-out regions, where the atmospheric transmittance is known to be zero. The fitted results and residuals of the same spectrum are shown in Figure 3.1(b) and (c). The curvature of the continuum is less than 0.2% judged from residuals, which is small compared with the uncertainty in the gaseous absorption.

Since atmospheric spectra have many saturated lines inside the O_2 A-band, even at the lowest air-mass, zero level offsets affect the retrieval heavily. An attempt of determining Z_{off} from the whole

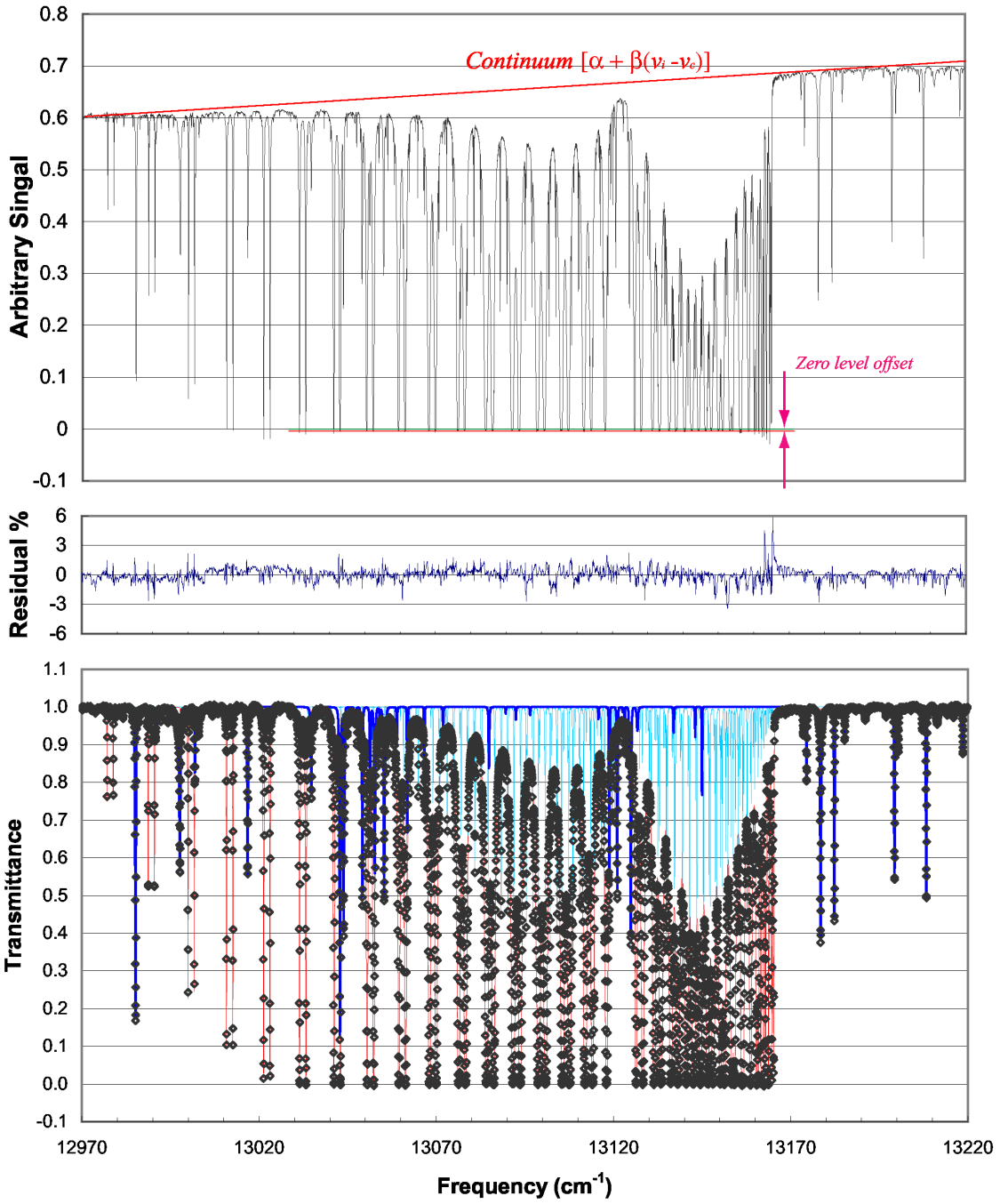

Figure 3.1: (a) A TMF O_2 A-band (12970~13220 cm^{-1}) spectrum measured at 51.50° SZA on March 24, 2003. The fitting parameters *continuum* and *zero level offset* are also shown. (b) the result of fitting the same spectrum in the same region. Diamonds are the measurements and black lines are calculated total transmittance. The contributions from $O^{16}O^{16}$, $O^{16}O^{16}$+$O^{16}O^{18}$, and the solar features are marked by red, cyan, and blue respectively. Compared with (a), the continuum has been normalized and the zero level offset has been subtracted. (c) the spectral fitting residual (measured minus calculated). The large peak at ~ 13165 cm^{-1} is probably caused by neglecting line-mixing.

A-band gives undue weight to spectral points that are nearly but not exactly blacked out. We thus retrieve zero levels separately from the contrast of non-absorbing and saturated regions inside the A-band, and input the results back into the general retrieval process to determine photon paths. The two-step strategy has reduced the scatter of retrievals from high airmass spectra, but slightly increased the scatter of the low airmass results. Study shows that, because of their narrower saturated regions and consequently larger sensitivity to other factors (e.g. ILS), it is difficult to determine Z_{off} for low airmass (<2) spectra. The retrieved Z_{off} values from these spectra scatter much more than the high airmass ones, and induce a spurious correlation between the retrieved scale factors and the Z_{off} themselves (not shown) after input into the 2^{nd} step retrieval. Nonetheless, a simple subtraction of this correlation reduces the scatter significantly, and is thus applied to retrievals from all low airmass spectra. The corrections are mostly around 0.1%, although a few can be as large as 0.3%.

A sensitivity test exhibits that the retrieved photon path scale factor from the A-band has temperature dependence that decreases almost linearly with airmass (from 0.16%/K at one airmass to 0.04%/K at seven airmasses). The positive temperature dependence indicates that the linewidth rather than the linestrength dominates the overall temperature sensitivity for this heavily saturated band. Since we only use one temperature profile for each day, the diurnal temperature variation at near ground levels could introduce significant error. For this reason, we retrieve the temperature at levels lower than 5 km using the contrast between the O_2 lines of different ground state energies as a correction. Tests using simulated spectra indicate that this strategy accurately retrieves O_2 at all airmasses, even when the a priori surface temperature is off by 10 K. This sensitivity test also demonstrated that the retrieved O_2 amount is not sensitive to the altitude-dependence of temperature change, as either a uniform offset or a top-fixed linear slope. We thereby use a simple offset T_{off} to change the temperature profiles at altitudes below 5km.

The positions, intensities, and ground state energies of the $O^{16}O^{16}$ A-band spectral absorption lines are from the HITRAN2000 [*Ritter and Wilkerson*, 1987; *Gamache et al.*, 1998] compilation

. The self- and pressure-broadening coefficients, however, were recalculated from a fit to several lab measurements [*Ritter and Wilkerson*, 1987; *Yang et al.*, 2000; *Brown and Plymate*, 2000; *Newman et al.*, 2000] (shown in Figure 3.2). In HITRAN2000, the widths of high rotational quantum number (denoted as J hereby) absorption lines were extrapolated from earlier measurements of the lower-J lines. The new linewidth estimates (the orange lines in Figure 3.2) substantially reduce the fit residuals especially for the high-J lines. Spectral parameters of $O^{16}O^{18}$ and $O^{16}O^{17}$ have also been updated [*Camy-Peyret*, private communication]. To avoid artifacts resulted from inconsistencies among the spectroscopic parameters of the various O_2 isotopomers, we retrieve separate scale factors for $O^{16}O^{16}$ and $O^{16}O^{18}$+$O^{16}O^{17}$, and use only the results from the $O^{16}O^{16}$ to determine photon paths.

Line mixing is only prominent for the high-J lines of the R branch band-head ($v \sim 13165$ cm^{-1}, shown in Figure 3.1), although *Linda Brown* [private communication] has speculated that it likely extends throughout the entire A-band. Since we do not have good technique to account for this effect, we only use the P branch ($v < 13120$ cm^{-1}) in spectral fitting. However, the non-absorbing regions on both sides of the A-band are used because they are necessary to derive the spectral continuum.

3.4 Results and discussion

Retrieved photon path scale factors (PPSF: ratios of the retrieved to geometrically derived ray paths) using Voigt function from $O^{16}O^{16}$ lines of the A-band FTUVS spectra are plotted versus the airmasses at which they are taken in Figure 3.3(a). The results are symmetrical in the morning and afternoon, demonstrating no existence of time offsets while recording these spectra. There is also no significant (< 0.1% in total) difference between the retrievals from the forward and reverse scannings (not shown). At a given airmass, the precision (1σ~ 0.2%) is satisfying, but the spurious correlation between the scale factors and the airmasses is obvious. An examination of the spectral

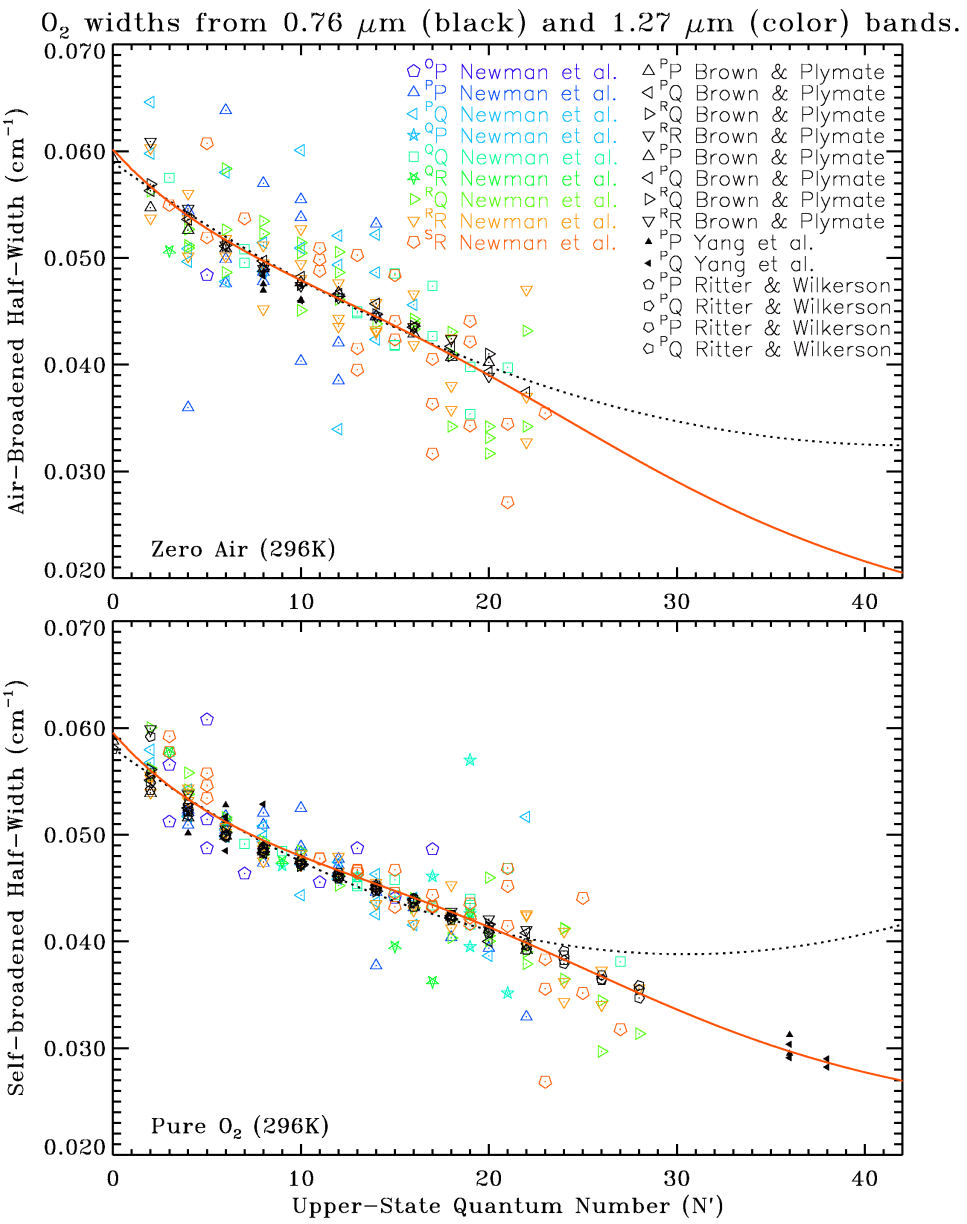

Figure 3.2: Laboratory measurements of air- and self- broadened half-width (ABHW and SBHW) of O_2 A-band (black) and O_2 1.27 um band (color) absorption lines from different references [*Ritter and Wilkerson*, 1987; *Yang et al.*, 2000; *Brown and Plymate*, 2000; *Newman et al.*, 2000]. The fit of the SBHW (orange line in panel (b)) to upper rotational quantum number (N') is

$$SBHW = 0.02204 + \frac{0.03749}{1 + 0.05428N' - 1.19 \times 10^{-3}N'^2 + 2.073 \times 10^{-6}N'^4} \tag{3.4}$$

and ABHW is then derived from SBHW (orange line in panel (a))

$$ABHW = 1.012\frac{SBHW}{\sqrt{1 + (\frac{N'-5}{55})^2}} \tag{3.5}$$

Both diverge from the HITRAN2000 extropolations (black dashed line) for $N' > 20$.

residuals (e.g. Figure 3.3(b) and (c)) reveals that the Voigt function gives too low a ratio of far wings to the near wings absorption. Changing linewidths in this formulation neither improves the residuals nor removes the airmass dependence. Considering the Dicke narrowing effect by adopting a hard collision model used to fit A-band lab spectra gives [*Ritter and Wilkerson*, 1987] indistinguishable results (not shown) from those of the Voigt lineshape, because Dicke narrowing affects only the line centers, which are blacked out for most of the O_2 lines considered here.

In an attempt to improve our retrievals, the super-Lorentz function described by *Hirono and Nakazawa* [1982] has been tested. This function is represented as:

$$f(v) = \frac{A(\eta)}{\pi} \frac{\gamma_L^{\eta-1}}{\{(v-v_0)^2 + \gamma_L^2\}^{\eta/2}} \tag{3.6}$$

where $\gamma_L$is the Lorentzian linewidth, v_0 is the absorption line center frequency, and $1 < \eta \leq 2$. is the normalization factor. When $\eta = 2$, $f(v)$ is Lorentzian; when $\eta < 2$, $f(v)$ becomes super-Lorentzian, i.e. weaker near the line center and stronger in the far wings (shown in Figure 3.4(a)). Although this lineshape is expected to better represent the dominant saturated lines in atmospheric A-band spectra, it provides a poorer representation of the line centers than the Voigt function because it neglects the Doppler effect. In this study, therefore, we apply the super-Lorentz function only to strong low-J (J $\leq$ 25) lines, which are always saturated at the centers for our spectra, and use Voigt function for other weak lines. Although the division is arbitrary, it gives smaller residuals than the attempt of combining two lineshapes (using Voigt for high altitudes and super-Lorentz for low altitudes) does.

The comparison of photon path scale factors retrieved using different choices of η are shown in Figure 3.4(b). As we use smaller η value (i.e. increase the far wing strengths), both the absolute value of retrieved scale factors and their airmass dependence decreases. In spite of this, there exists no single η value that completely removes the airmass dependence. For example, at η = 1.977 (which gives the smallest rms for super-Lorentz function fits), the low airmass (<1.8) retrievals are almost

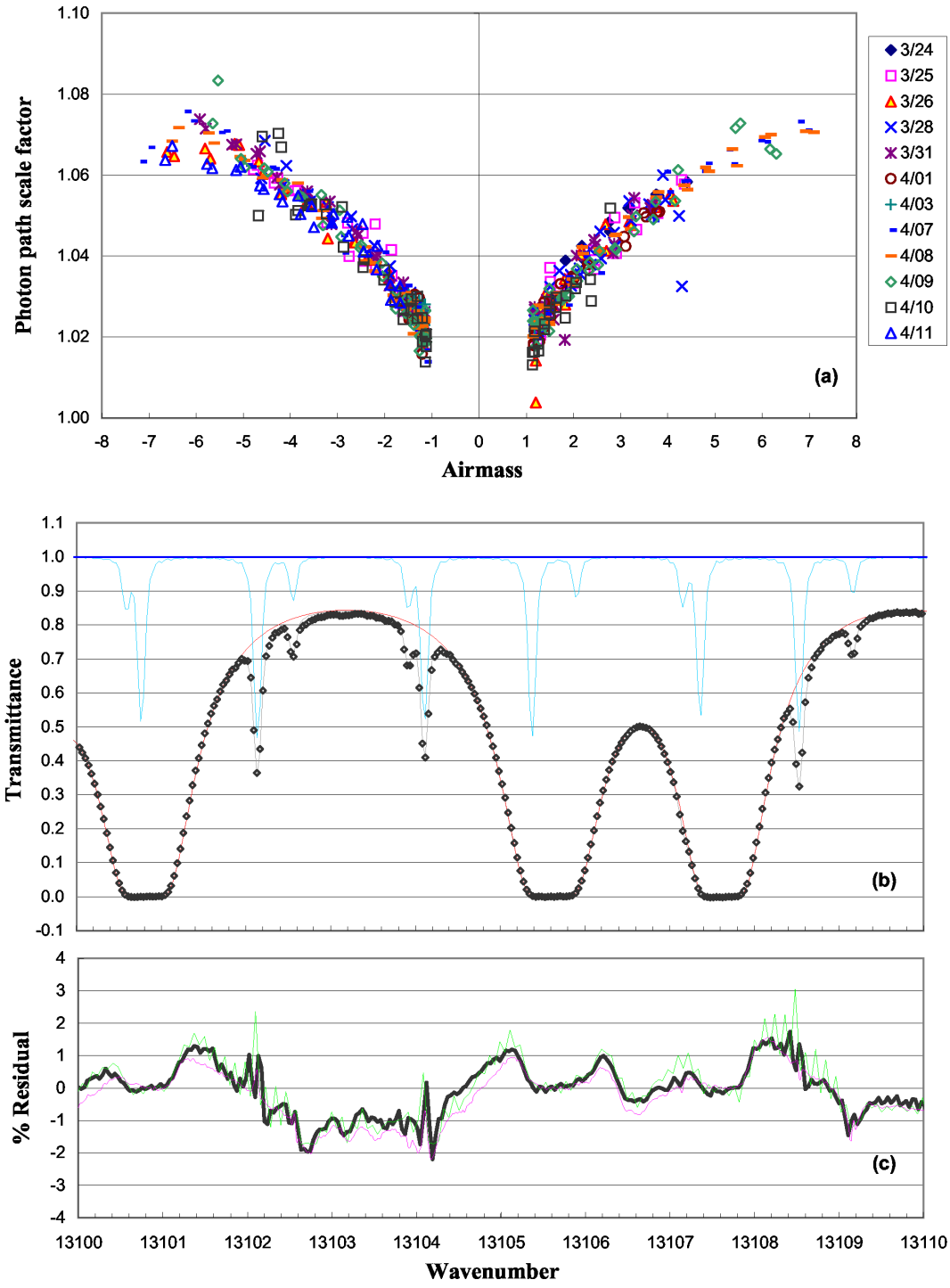

Figure 3.3: (a) Photon path scale factors retrieved from the TMF spectra using Voigt lineshape plotted versus the airmasses at which they were taken. Negative and positive airmasses mean the spectra were taken in the morning and afternoon, respectively. Each day's results are marked differently. (b) An expanded view of the $13100 - 13110$ cm^{-1} region for the same TMF spectrum shown in Figure 3.1. (c) The spectral fitting residual of (b) (black line) together with residuals from fitting a Kitt Peak spectrum (pink line) and a Caltech spectrum (green dash line), demonstrating that the error pattern is not of instrumental origin.

airmass-independent, but the other retrievals still increase with airmass; and when η = 1.958, the fitting rms is larger (but still smaller than those of Voigt function), the airmass-independent region moves to modest airmasses (2.5 ~ 4), while low and high airmass retrievals show negative and positive airmass dependences respectively. An investigation of the fitting residual of saturated lines (not shown) reveals that, compared with the Voigt lineshape, the super-Lorentz lineshape represents the far wings better, but still has the same problem of overestimating the near wings (from line center to ~1.5 cm^{-1} away), which might be a result of neglecting line-mixing. Besides, this overestimation gets worse for high airmass spectra, which should be responsible for the complex airmass dependences of retrievals. Considering the 2% accuracy of line intensities [*Ritter and Wilkerson*, 1987; *Brown and Plymate*, 2000], η = 1.977 gives the most reasonable absolute values (0.97~1.00, should be unity). Nevertheless, without accurate laboratory information on the far-wing lineshape, it is impossible to ascertain if the retrieved non-unity scale factors are the result of spectroscopic, instrumental, or other errors.

The observed airmass dependence can not be explained by errors introduced by the use of discrete levels in the ray path calculation. We compared our 70-level-discretized calculations of airmass with results of a numerical integration [*Kristensen*, 1998], both using the International Civil Aviation Organization (ICAO) standard atmosphere. The discrete calculation gives smaller photon paths, and the absolute difference increases almost linearly with airmass. However, the differences (shown in Figure 3.5, ~0.13% at one airmass and ~0.02% at seven airmasses) are small compared with the variance in O_2 scale factors shown in Figure 3.4(b). Moreover, correcting the ray-tracing error will worsen the spurious correlation between airmass and retrieval photon path, if we use Voigt lineshape or super-Lorentz lineshape of η value larger than 1.977.

Evaluation of achievable precision from current spectral retrieval technique is based on the scatter of the ”flat region” in Figure 3.4(b), analyzed using super-Lorentz function of η= 1.977. For 230 TMF spectra taken at airmasses less than 1.8 (Figure 3.6), the mean of retrieved scale factors is 0.9777 and the 1σ is 0.0022, sufficient to fulfill the requirement of calibrating 0.3% change in

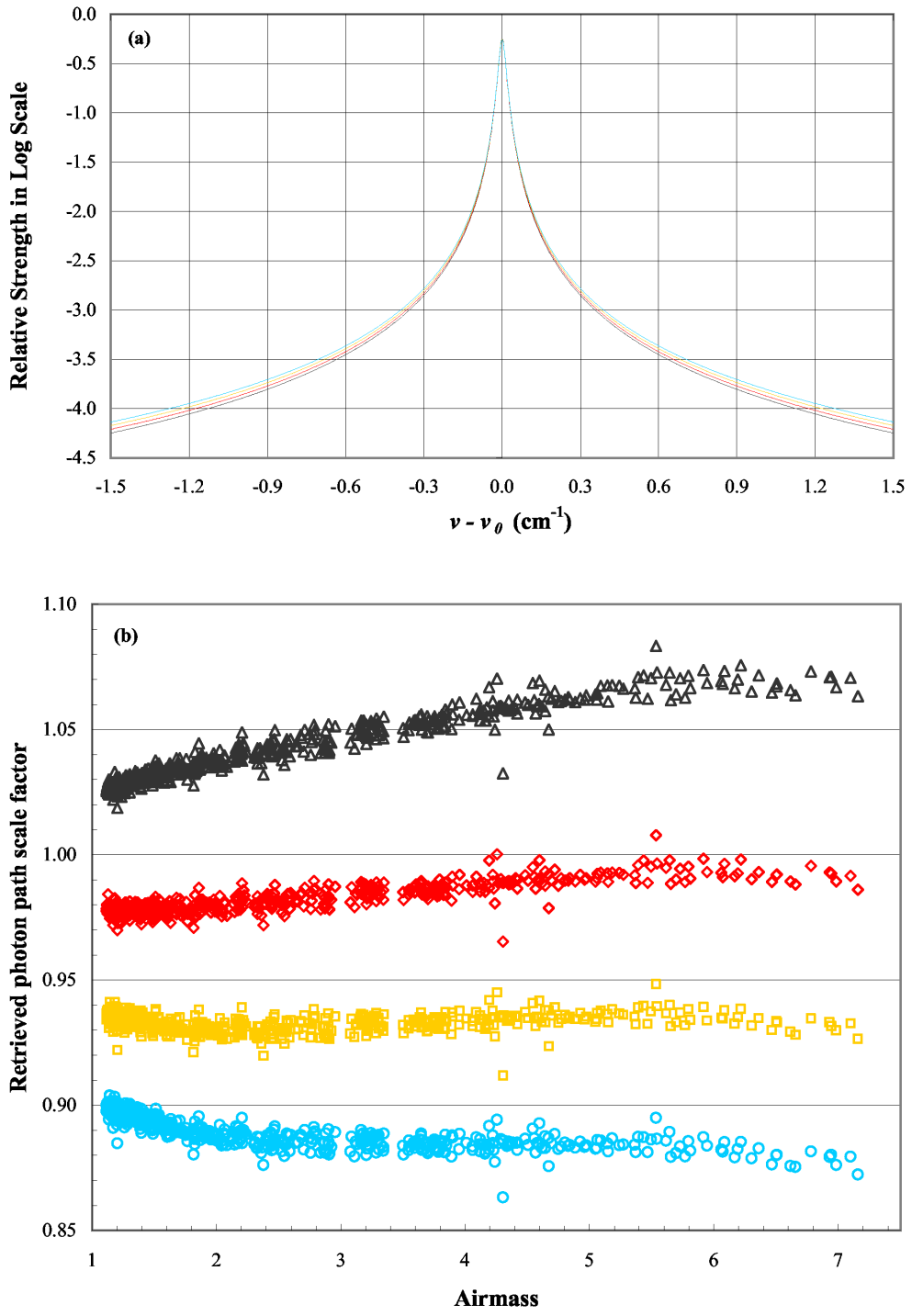

Figure 3.4: (a) The comparison of Lorentz lineshape function (approximating Voigt function in the wings, in black) and super-Lorentz function with η = 1.977 (red), 1.958 (brown), and 1.940 (light blue), assuming a 0.015 cm^{-1} Doppler width. The strength axis is in log scale. The far wing absorption clearly increases with decreasing η. The differences in the center are small and immaterial because the strong lines are saturated there. (b) Retrieved photon path scale factors using different lineshape functions versus airmass, using the same color scheme as in (a).

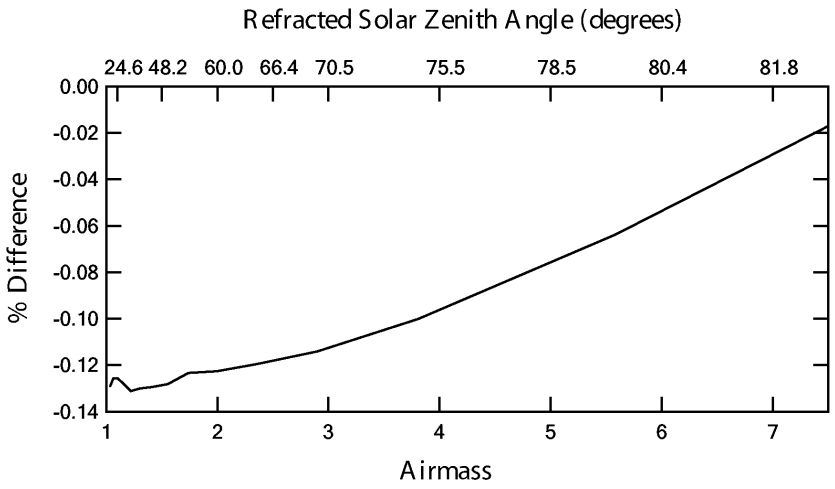

Figure 3.5: Denote the integrated aimass from *Kristensen* [1998] as AM_{Kri} and our 70-level discretized atmosphere calculation as AM_{dis}. The relative difference between the two is defined as

$$\%Difference = 100 \times \frac{AM_{dis} - AM_{Kri}}{AM_{Kri}} \tag{3.7}$$

and plotted versus both airmass and refracted solar zenith angle.

atmospheric CO_2 over this relatively small variation in surface pressure (~10 mbar). Observations made over a broader range of surface pressures would be helpful to further test the retrieval and could provide further insight about the physics of absorption in the A-band. In addition, in these mountain top observations, the water vapor column is small. This clearly will not be the case for soundings made at higher pressure. Because the influence of H_2O on the lineshape is unknown, further retrieval error can be expected.

Although the super-Lorentz lineshape is imperfect for describing A-band lines, its better representation of the far wings may indicate the existence of collision-induced absorption (CIA), which was previously speculated [*Mlawer et al.*, 1998]. According to the statistical theory, super-Lorentz function of $\eta = 2$ corresponds to dipole-dipole (e.g. O_2-O_2 or O_2-N_2) interaction and that of $\eta = 1.75$ corresponds to dipole-quadrupole (e.g. O_2-O_4) interaction , so that the super-Lorentz lineshape of in-between η values represents the mix of common absorption and CIA. Then again, the very small intensity of CIA in this region is immeasurable without extremely long path cell

in the lab. To derive the CIA from atmospheric spectra, by finding a lineshape function (could be similar to the multi-variable CKD model described by *Clough et al.* [1989]) that minimizes the airmass dependence of the retrievals instead of absolute rms error of an individual fit, might be possible but difficult.

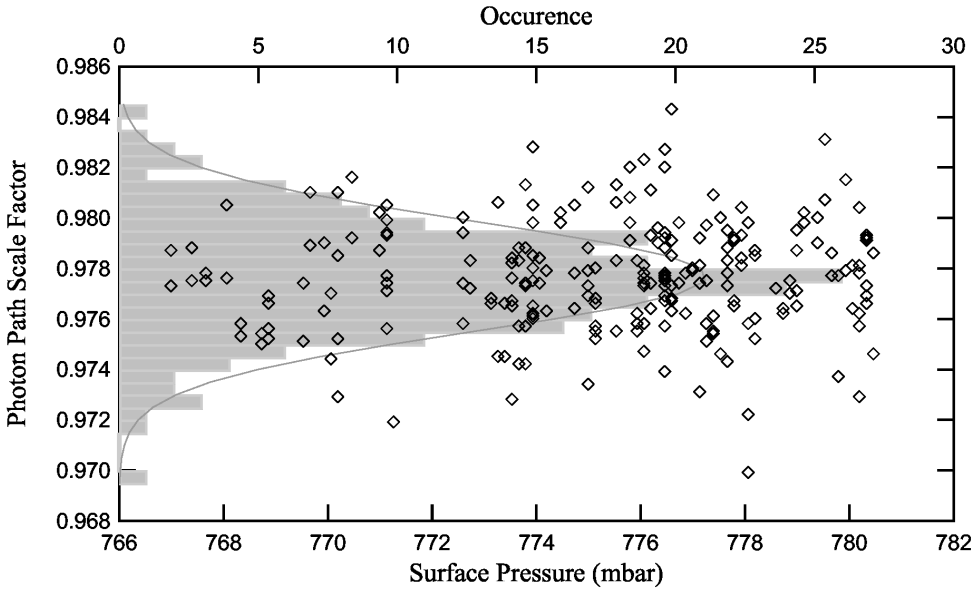

Figure 3.6: Retrieved photon path scale factors from the low airmass (<1.8) spectra using η = 1.977 super-Lorentz function versus surface pressures at which they were taken. Corresponding histogram and the fitted Gaussian curve are in the background.

3.5 Conclusion

Using ground-based measurements of direct sunlight as a simple test, we have shown that photon paths can be retrieved with high precision (~0.2%) from high resolution FTS solar absorption spectra of the O_2 A-band, over a significant SZA driven (but not surface pressure) variation in airmass. This is achieved by virtue of: 1) the atmospheric O_2 being extremely well mixed with an accurately known mole fraction; 2) the A-band lines being strong, numerous, and almost free of absorption by other gases; 3) the stable and self-calibrating nature of the FTS instrument; 4) the high signal-to-noise-ratio of direct solar absorption spectra. Successful retrieval of photon paths

will eliminate a major systematic error source of future remote sensing experiments using solar radiation as a light source, and greatly improve their precision in measuring many tropospheric species.

The major obstacle for further progress in this effort is that we cannot correctly represent the line-shape of the absorption in the A-band. Error in this parameterization results in spurious correlation between retrieved photon path scale factors and the airmasses at which the spectra were taken. Neither Voigt nor super-Lorentz lineshape is the correct description for the strong absorption lines in the A-band. Although we speculate that the near wing overestimation and the far wing underestimation could be due to line-mixing and continuum absorption respectively, it is difficult to unambiguously determine the reasons for the poor spectral fits of open-path atmospheric spectra because there are too many unknowns (interfering absorption features, T/P varying along the line of sight, etc.). New laboratory measurements of the O_2 A-band lineshape with a closed-path of at least 10 km are clearly needed.

Chapter 4

Using column CO_2 mixing ratio to constrain North Hemispheric Net Ecosystem Exchange[1]

Abstract

We present the first effort to use column CO_2 to constrain the global carbon budget. This analysis uses observations of the column-averaged dry molar mixing ratio of CO_2 above both Park Falls, Wisconsin and Kitt Peak, Arizona, together with partial columns derived from six aircraft profiles over Eurasia and North America to estimate the seasonal integral of net ecosystem exchange (NEE) between the atmosphere and the terrestrial biosphere in the Northern Hemisphere. We find that NEE is approximately 28% larger than predicted by the Carnegie Ames Stanford Approach (CASA) model. We show that the earlier estimates of NEE may have been biased low by too weak vertical mixing in the transport models used to infer seasonal changes in Northern Hemisphere CO_2 mass from the measured surface CO_2.

[1]Adapted from Z. Yang, R. A. Washenfelder, G. Keppel-Aleks, N. Y. Krakauer, J. T. Randerson, P. P. Tans, C. Sweeney, and P. O. Wennberg (2007), New constrains on Northern Hemisphere growing season net flux, *Geophysical Research Letters*, 34, L12807, doi:10.1029/2007GL029742

4.1 Introduction

Forecasting future CO_2 levels in the atmosphere is needed to predict future climate. Accurate forecasts require an improved understanding of carbon sources and sinks [*IPCC*, 2007]. During the 1990s, fossil fuel combustion and cement production added approximately 6 PgC/yr to the atmosphere. These fluxes are well constrained spatially and temporally [*Andres et al.*, 1996]. From the observed atmospheric increase and the known anthropogenic emissions, the combined ocean and terrestrial biosphere carbon sinks must have been close to 3 PgC/yr [*IPCC*, 2007].

To estimate the spatial and temporal distribution of these carbon sinks, inverse methods have been used to estimate carbon fluxes from geographically sparse observations of atmospheric CO_2 mixing ratio, typically measured at the surface (e.g. *Tans et al.* [1990]). In these methods, surface fluxes are scaled within the framework of a global atmospheric transport model to minimize the difference between the observed and simulated spatial and temporal gradients of atmospheric CO_2 mixing ratio [*Enting et al.*, 1995; *Kaminski et al.*, 1999; *Rayner et al.*, 1999; *Bousquet et al.*, 2000; *Krakauer et al.*, 2004; *Baker et al.*, 2006]. Estimates of both NEE and the geographical distribution of fossil fuel carbon sinks vary significantly, due in large part to errors in the atmospheric transport models used in these inversions (e.g. *Gurney et al.* [2004]). This is quite understandable; estimation of fluxes on large geographical scales requires knowledge of temporal and spatial gradients in CO_2 mass. These changes in mass can be inferred from gradients in the observed mixing ratio at the surface only if the vertical structure of atmospheric CO_2 is well known. Proper simulation of the exchange between the planetary boundary layer (PBL) and the free troposphere, however, is still an area of active research for the atmospheric dynamics community.

In this study, we use newly available observations of the column and vertical profile dry air CO_2 molar mixing ratios above eight sites (Table 4.3) to estimate the seasonally-varying carbon flux (NEE) in the northern hemisphere. Because these observations are of the column abundance, they come close to representing directly a measure of atmospheric CO_2 mass. As a result, our estimate of NEE is significantly less sensitive to errors in the vertical transport than estimates based solely

on surface observations. Our analysis suggests that the seasonally-varying fluxes are substantially larger than the NEE fluxes from the CASA model used in the *TransCom 3* studies. We show using vertically resolved observations of CO_2 obtained at several sites in Eurasia and North America that the TransCom models underestimate the seasonally-varying fluxes because they underestimate the efficiency of mixing of CO_2 throughout the free troposphere.

4.2 Measurements and Models

Measurements of column-averaged dry CO_2 were obtained at Park Falls, Wisconsin beginning in 2004. Using an automated solar observatory, direct solar spectra were acquired continuously during clear-sky, daytime conditions. These spectra were used to determine vertically integrated CO_2 mass with high precision (0.1%) [*Washenfelder et al.*, 2006]. The 337 days of measurements were taken during May 2004 to November 2006 and have been averaged daily. We also included similar but much infrequent (only 96 days during two periods: January 1979 to December 1985 and March 1989 to March 1995) column measurements obtained at the Kitt Peak solar observatory, Arizona [*Yang et al.*, 2002]. In addition to the ground-based total columns, multi-level aircraft CO_2 measurements were available at six sites in North America and Eurasia during 2003-2004 (4.3 on page 53). Discrete CO_2 samples were acquired biweekly or monthly up to 7500 m above the surface (e.g. *Levin et al.* [2002]). In our analysis, we used the interpolations of these measurements at fixed temporal (48 per year) and spatial (every 500m in altitude) intervals [*GlobalView-CO_2*, 2006].

To compare with the observations, we used the twelve TransCom 3 experiment models that differ in spatial resolution, advection scheme, driving winds, and sub-grid scale parameterizations [*Gurney et al.*, 2003]. Monthly terrestrial biosphere exchange ($1^\circ \times 1^\circ$) was derived from the Carnegie-Ames-Stanford Approach (CASA) terrestrial biosphere model [*Randerson et al.*, 1997], and is annually balanced at each grid cell.

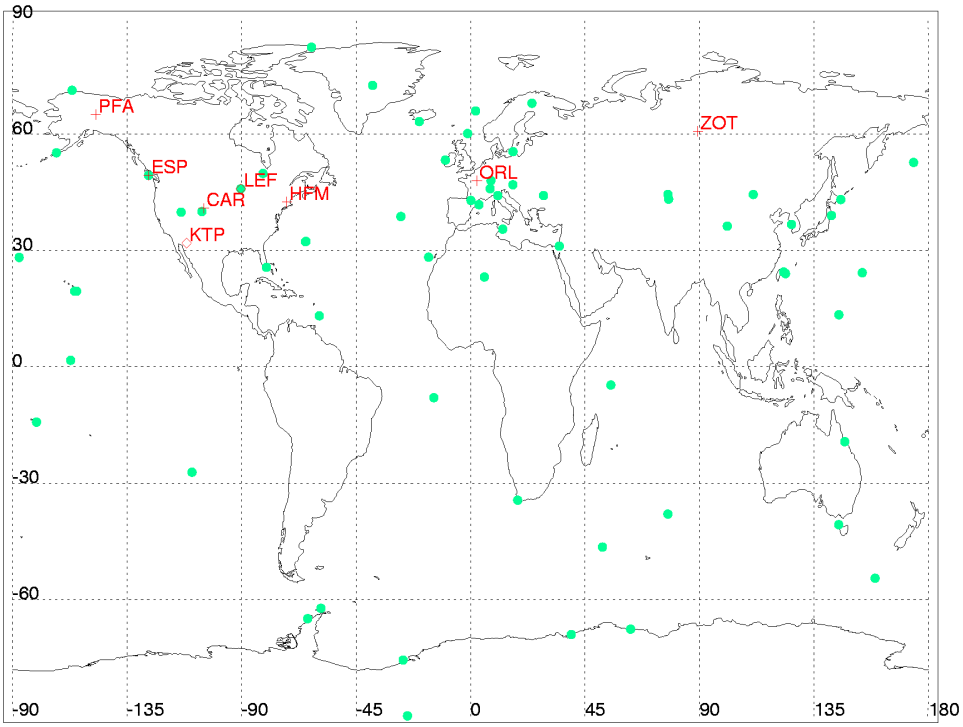

Figure 4.1: The locations of all data sites used, including both column/partial-column (red crosses with code names) and surface CO_2 observations (green dots). For surface sites, only those between 30°N–70°N are included in my analysis.

4.3 Methods

In our analysis, we compared the observed amplitude and phase of the atmospheric CO_2 seasonal cycles to simulations obtained from propagating seasonal surface fluxes from a terrestrial biosphere model (CASA) with annually-balanced fluxes through the twelve different transport models. Since the same fluxes are used, differences in the simulated atmospheric CO_2 seasonal cycles at different altitudes and locations become a comparative measure of differences in transport in the models. To quantify the differences between the observations and the simulations, we used a simple least square fit, assuming the observed seasonal cycle S(t) was a function of the simulated CASA biosphere model response $S_0(t)$, adjusted by scale factor A, time delay T, and offset B:

$$S(t) = A \times S_0(t - T) + B \tag{4.1}$$

Focusing on the shape of seasonal cycle, we reported A and T but not offset B. The parameters A and T can also be thought of as two spatially uniform adjustments to all CASA surface fluxes because of the linear relationship between these fluxes and S(t). Besides the simulations from the twelve models, the mean of all these models' simulations was considered as our "best" estimate and included in the comparison. The fitting rms (σ) for the all-model mean simulation was reported to measure the goodness of the fit, and to derive a weighted mean CASA scale factor (but not time delay) for *n* different sites:

$$\overline{A} = \frac{\sum_{i=1}^{n} A_i/\sigma_i^2}{\sum_{i=1}^{n} 1/\sigma_i^2} \tag{4.2}$$

To compare the observations with the neutral biosphere simulations, the measurements had been detrended and offset by the annual mean value. The interannual trend for the Park Falls column CO_2 was empirically determined as 1.80 ppmv/yr during 2004 to 2006. For Kitt Peak, the trends were 1.41 ppmv/yr during 1979 to 1985 and 0.83 ppmv/yr during 1989 to 1995. For the temporally

evenly spaced GlobalView assimilations, their seasonal cycles were directly decomposed using the empirical mode decomposition method [*Huang et al.*, 1998] and folded into one year.

4.4 Results and Discussion

The comparison between the Park Falls CO_2 seasonal cycle of column-averaged observation and the TransCom simulations is shown in Figure 4.2. The observed seasonal CO_2 cycle amplitude is larger than any model simulation. A best fit was obtained by increasing the CASA fluxes by 34%. Models also underestimated the CO_2 seasonal cycle at Kitt Peak and all the other six aircraft sites (average difference of 27%, Table 4.3). Because these vertically-integrated observations sample a significant fraction of the northern hemisphere landmass, they provide a measure of CO_2 mass variations that is not highly sensitive to error in the transport fields. As a group, the seasonal cycle in column CO_2 is most sensitive to the seasonal fluxes themselves. This is supported by the relatively small variation in the model simulations of the columns illustrated for Park Falls in Figure 1 and for the other sites in the accompanying supplementary material.

The NEE used in CASA was derived from 1990 satellite observations, and so the observed 0.66%/yr increase rate of CO_2 seasonal-signal amplitude between 1981 to 1995 [*Randerson et al.*, 1997] may explain some, but clearly not all, of the differences between the observations and simulations of the amplitude of the CO_2 seasonal cycle. In addition, the phase analysis of CO_2 seasonal cycles shown in Table 1 shows that for all sites except Kitt Peak, CASA fluxes needed to be shifted earlier by one to three weeks, which may, in part, be explained by advances in the timing of spring thaw since 1988 [*Smith et al.*, 2004].

In contrast to the column results, comparison of the simulations of the seasonal cycle with CO_2 observations obtained at the surface [*GlobalView-CO_2*, 2006] between 30°N to 70°N shows both a smaller under-estimation of seasonal cycle (~12%, Table 4.3) and a smaller phase delay ($T_{surface}$ = -11.9 days; T_{column} = -14.5 days). Both the amplitude and phase differences between the estimates

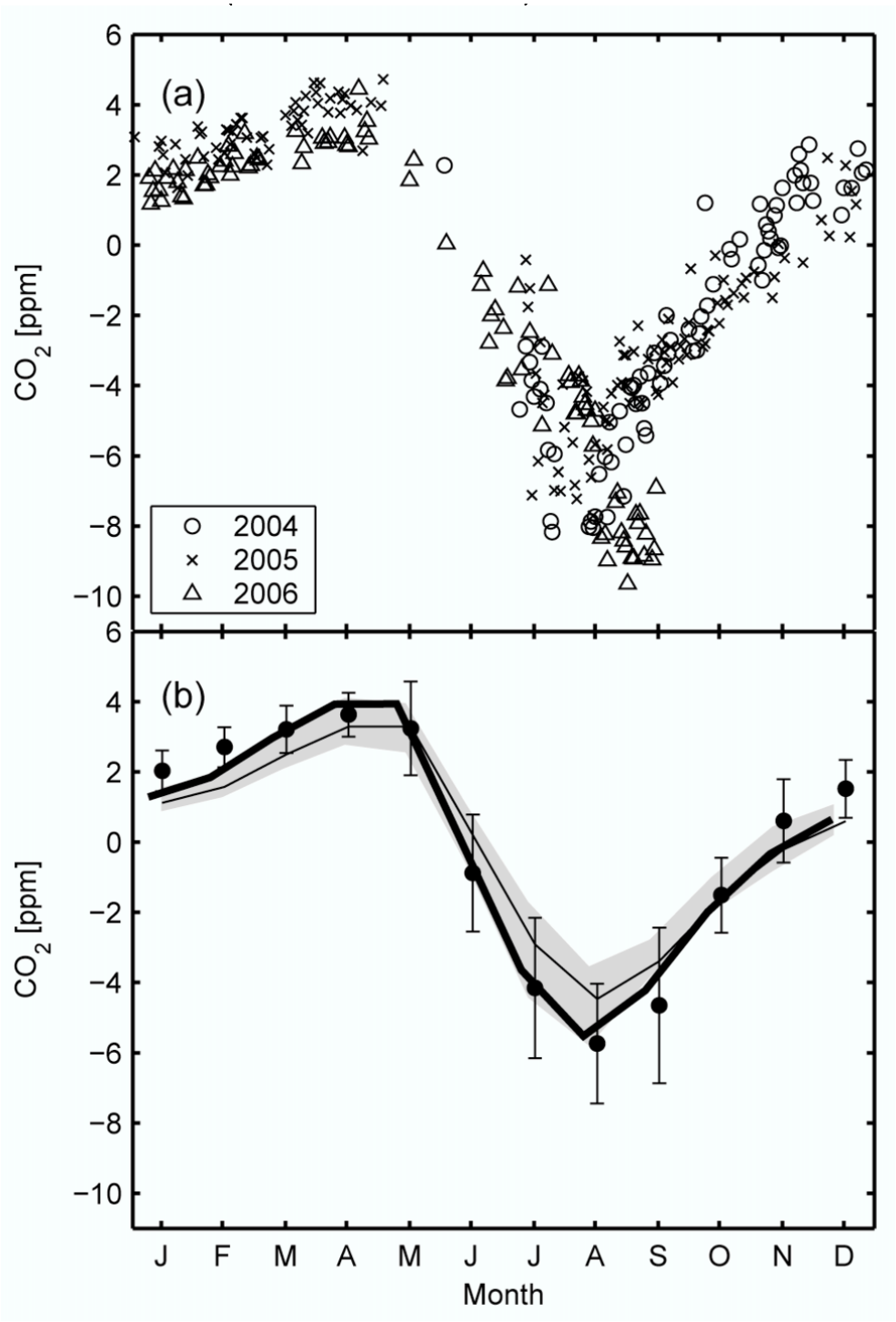

Figure 4.2: (a) Atmospheric column-average CO_2 mole fractions at Park Falls for May 2004 ~ March 2006. (b) The monthly mean of observations (close circles) compared with the TransCom simulations (grey shade shows range of 12-model predictions; thin solid line represents average; thick solid line is the best fit). Each of the 12 models under-predicts the seasonal cycle observed in the column measurements. The best match to the observations is achieved by scale the model-mean simulations by 1.34 and shift them 7 days earlier.

from surface and column observations suggest that the TransCom models as a group do not mix the surface fluxes into the free troposphere quickly enough.

To investigate vertical mixing in the models, we focused on altitude-resolved data from the six aircraft sites. The results of such an analysis are shown in Figure 4.5: the relationship between retrieved CASA scale factors and altitude for are quite different from site to site. We find that direct comparison between the simulations and observations for these sites was hampered by large mismatches in the shape of the CO_2 seasonal cycle at some sites (e.g. ZOT in Figure 4.6 on page 55), and a new diagnostic method is necessary.

To minimize the impact of the seasonal-signal shape mismatch we performed self-similarity tests separately for observations and model simulations, among their seasonal cycles at different altitudes. For each site, we defined a reference level and assumed the seasonal cycles S(t) at any level could be represented by this reference seasonal cycle $S_{ref}(t)$ with a time delay *T* (due to vertical mixing), amplitude scale factor *A*, and offset *B*, where S(t) and $S_{ref}(t)$ must be of the same type (simulation or observation):

$$S(t) = A \times S_{ref}(t - T) + B \tag{4.3}$$

The 3500 m level was chosen as the reference for all sites. The comparison for each site is shown in Figure 4.6 and the retrieved values of *A* and *T* are listed in Table 4.4. For the model simulations at all sites, the scale factors monotonically decrease with altitude, while the time delays monotonically increase. In contrast, for the observations at or above 2500 m, all sites except ESP showed slower decreases or even increases in the amplitude scale factor with altitude as well as shorter delay, and even advance (at PFA) in the seasonal cycle phase. For levels below 2500 m, the observations showed mixed trends from site to site, again possibly influenced by strong PBL variation. The observation-model differences above 2500m strongly suggest that the atmospheric vertical and/or meridional mixing within the free troposphere is faster than the TransCom simulations.

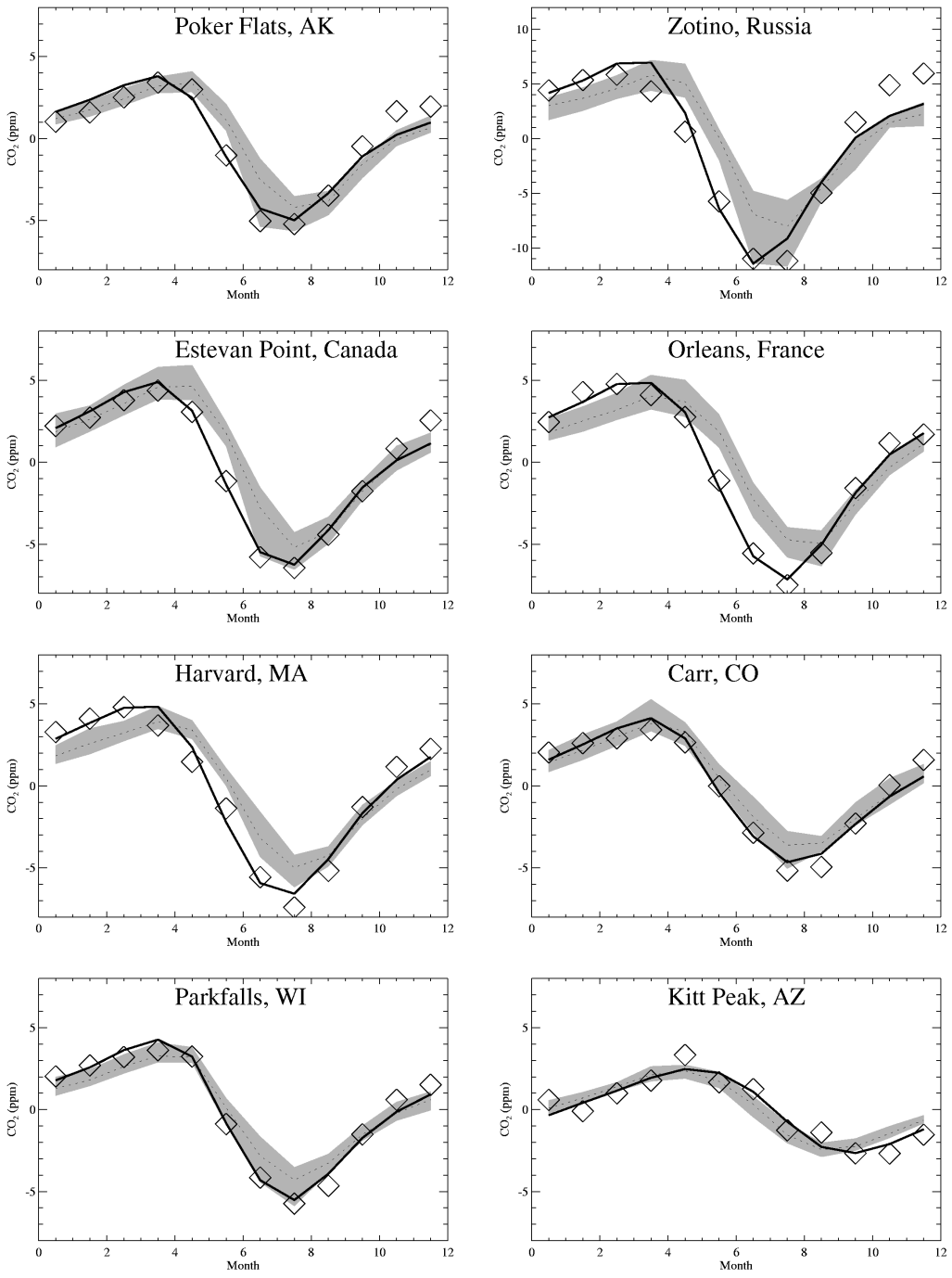

Figure 4.3: The monthly mean of observations (open diamonds) compared with the TransCom simulations for each of the eight sites. In each figure, grey shade show range of 12-model predictions, thin dotted line represents average, and thick solid line is the best fit with scaling and shifting.

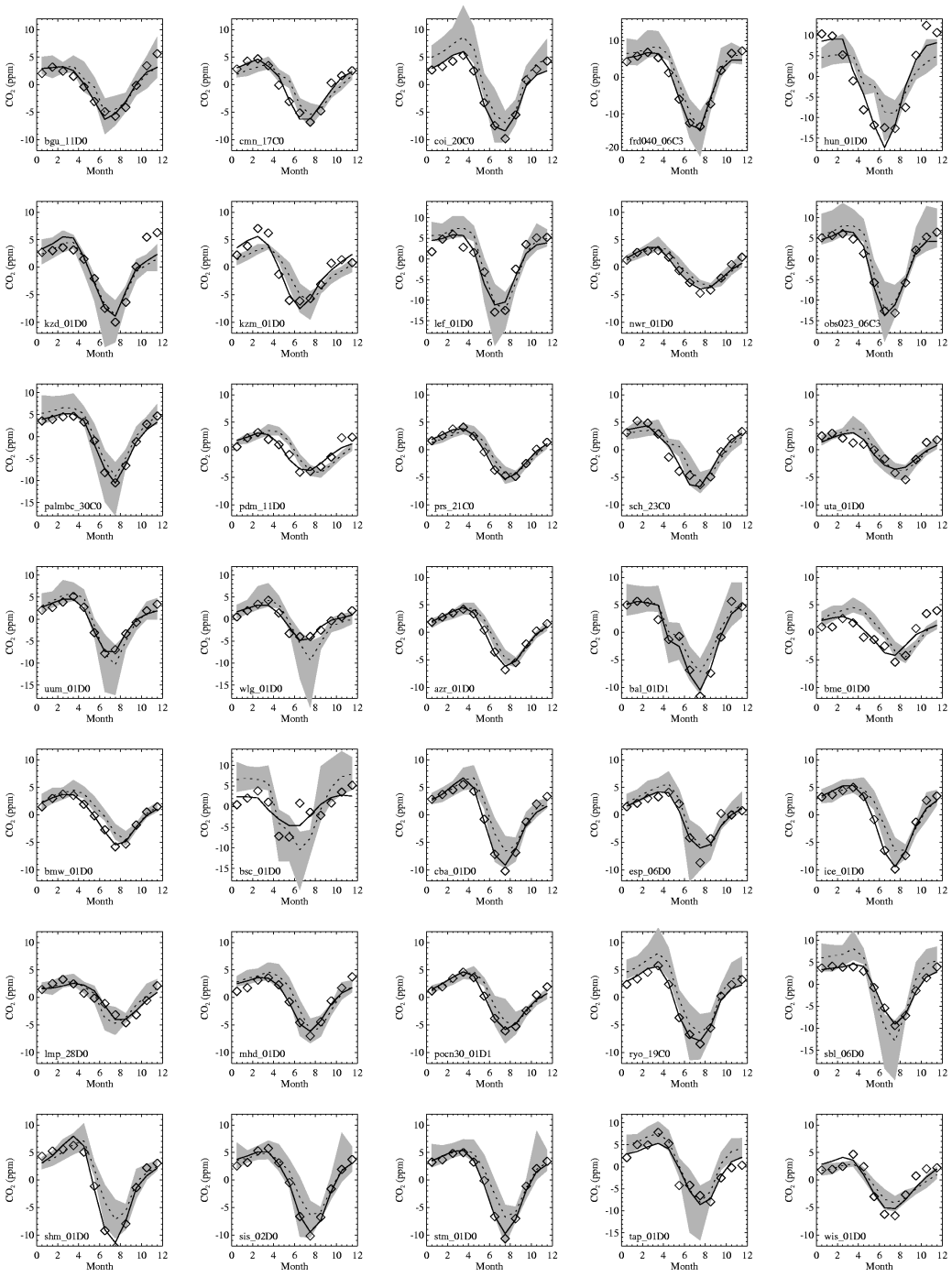

Figure 4.4: The monthly mean of observations (open diamonds) compared with the TransCom simulations for each of the 35 surface sites. Denotations are the same as in Figure 4.3. The detailed results for the surface site are listed in Table 4.1.

Table 4.1: The analysis detail of 35 surface sites

Site	Type*	Location	Altitude (m)	Mean scale factor A of the 12 models	Mean phase shift T (in days) of the 12 models	Scale factor A for the mean responses of 12 models	Phase shift T (in days) for the mean response of 12 models	RMS in fitting the mean response of 12 models (ppm)
bgu_11D0	L	41.8°N, 3.3°E	30	1.22± 0.34	-13.08±10.89	1.25	-11.00	0.90
frd040_06C	L	49.9°N, 81.6°W	250	1.06± 0.27	-9.83± 2.41	1.02	-9.0	1.05
hun_01D0	L	47.0°N, 16.6°E	344	2.01± 0.54	-19.67± 5.88	1.94	-18.0	3.14
kzd_01D0	L	44.5°N, 77.6°E	412	1.18± 0.19	-3.83± 7.58	1.16	-3.0	2.13
kzm_01D0	L	43.2°N, 77.9°E	2519	1.42± 0.16	-23.08± 4.68	1.43	-24.0	1.21
lef_01D0	L	45.9°N, 90.3°W	868	0.95± 0.21	-10.50± 3.50	0.92	-9.0	1.92
nwr_01D0	L	40.0°N, 105.6°W	3475	1.10± 0.11	-17.58± 7.06	1.12	-17.0	0.55
obs023_06C	L	54.0°N, 105.1°W	652	1.05± 0.30	-6.92± 5.66	1.00	-6.0	1.20
palmbc_30C	L	68.0°N, 24.1°E	560	1.02± 0.28	-1.92± 6.16	0.96	0.0	0.64
pdm_11D0	L	42.9°N, 0.1°E	2877	0.96± 0.12	-33.33± 3.68	0.96	-35.0	0.86
prs_21C0	L	45.9°N, 7.7°E	3480	1.22± 0.15	-17.00± 3.30	1.23	-17.0	0.27
sch_23C0	L	48.0°N, 8.0°E	1205	1.33± 0.22	-20.42± 5.30	1.34	-19.0	1.03
uta_01D0	L	39.9°N, 113.7°W	1320	0.88± 0.13	-12.25± 8.70	0.89	-12.0	1.27
uum_01D0	L	44.5°N, 111.1°E	914	0.87± 0.24	-10.33± 3.28	0.83	-9.0	0.77
wlg_01D0	L	36.3°N, 100.9°E	3810	0.75± 0.19	-21.67± 6.05	0.71	-20.0	0.83
azr_01D0	O	38.8°N, 27.4°W	40	1.15± 0.16	-15.00± 4.47	1.15	-15.0	0.37
bal_01D1	O	55.5°N, 16.7°E	7	1.20± 0.29	1.00± 9.40	1.16	1.0	1.19
bme_01D0	O	32.4°N, 64.7°W	30	0.69± 0.15	-32.58± 3.75	0.68	-33.0	1.55
bmw_01D0	O	32.3°N, 64.9°W	30	1.00± 0.18	-11.58± 4.58	1.00	-11.0	0.41
bsc_01D0	O	44.2°N, 28.7°E	3	0.37± 0.16	-24.92± 8.73	0.36	-21.0	2.52
cba_01D0	O	55.2°N, 162.7°W	25	1.22± 0.26	-12.75± 4.45	1.20	-12.0	0.80
esp_06D0	O	49.4°N, 126.6°W	39	0.90± 0.21	-8.67± 7.30	0.88	-7.0	1.12
ice_01D0	O	63.2°N, 20.1°W	100	1.26± 0.23	-16.50± 5.82	1.25	-16.0	0.58
lmp_28D0	O	35.5°N, 12.6°E	45	0.97± 0.14	11.58± 7.69	0.99	11.0	0.84
mhd_01D0	O	53.3°N, 9.9°W	25	0.93± 0.19	-18.00± 8.50	0.94	-18.0	0.90
pocn30_01D	O	30.0°N, 126.0°W	10	1.08± 0.17	-16.42± 6.33	1.10	-15.0	0.39
ryo_19C0	O	39.0°N, 141.8°E	260	0.99± 0.20	-11.00± 3.36	0.97	-10.0	0.49
sbl_06D0	O	43.9°N, 60.0°W	5	0.72± 0.20	9.92± 3.78	0.69	10.0	0.43
shm_01D0	O	52.7°N, 174.1°E	40	1.42± 0.28	-10.92± 4.19	1.40	-10.0	0.90
sis_02D0	O	60.2°N, 1.2°W	30	1.28± 0.22	-9.75± 8.25	1.29	-9.0	0.65
stm_01D0	O	66.0°N, 2.0°E	7	1.23± 0.24	-10.42± 6.47	1.22	-9.0	0.47
tap_01D0	O	36.7°N, 126.1°E	20	0.93± 0.25	7.83± 5.70	0.89	8.0	1.89
wis_01D0	O	31.1°N, 34.9°E	400	1.47± 0.15	-13.08± 9.70	1.51	-12.0	1.37

*L for land sites and O for ocean sites

Table 4.3: Column and profile observation sites and the CO_2 seasonal cycle amplitude comparison with model simulations

Site Name (Code)	Location	Altitude range above surface (m)	Mean scale factor *A* of the 12 models[a,b]	Phase Shift *T* of 12 models (days)	Scale factor *A* for the mean response of the 12 models	RMS in fitting the mean response of the 12 models (ppm)
Poker Flats, AK (PFA)	65.07°N, 147.29°W	1500-7500	1.20±0.11	-16.8±4.5	1.21	0.71
Zotino, Russia (ZOT)	60.75°N, 89.38°E	500-3500	1.44±0.21	-18.4±2.8	1.42	1.70
Estevan Point, Canada (ESP)	49.38°N, 126.55°W	500-5500	1.20±0.12	-16.0±3.2	1.20	0.54
Orleans, France (ORL)	47.80°N, 2.50°E	500-3500	1.39±0.18	-19.6±3.1	1.38	0.43
Park Falls, WI (LEF)	45.93°N, 90.27°W	Total column	1.34±0.14	-7.3±4.0	1.34	0.43
Harvard Forest, MA (HFM)	42.54°N, 72.17°W	500-7500	1.38±0.09	-16.0±2.7	1.38	0.67
Carr, CO (CAR)	40.90°N, 104.80°W	1500-6500	1.20±0.11	-7.6±7.3	1.21	0.56
Kitt Peak, AZ [c] (KTP)	31.90°N, 111.60°W	Total column	1.11±0.07	15.3±4.6	1.12	0.56
Mean			1.28	-14.5±5.0 [d]	1.28	0.70
Mean of 35 surface sites [e] in 30°N~70°N			1.12	-11.9±9.8	1.11	1.07

[a] For LEF and KTP, total CO_2 columns were simulated for the comparison. For the aircraft sites, only partial columns with measurements were simulated. The scale factor A and phase shift T here are described by Equation 4.1.
[b] The name of the models are CSU.gurney, GISS.prather, GISS.prather2, GISS.prather3, JMA-CDTM.maki, MATCH.bruhwiler, MATCH.chen, MATCH.law, RPN.yuen, SKYHI.fan, TM3.heimann, GCTM.baker.
[c] The Kitt Peak observations were taken from January 1979 to March 1995, for more detail refer to *Yang et al.* [2002].
[d] Excluding Kitt Peak due to different observation time period.
[e] The 35 surface sites are listed in Table 4.1.

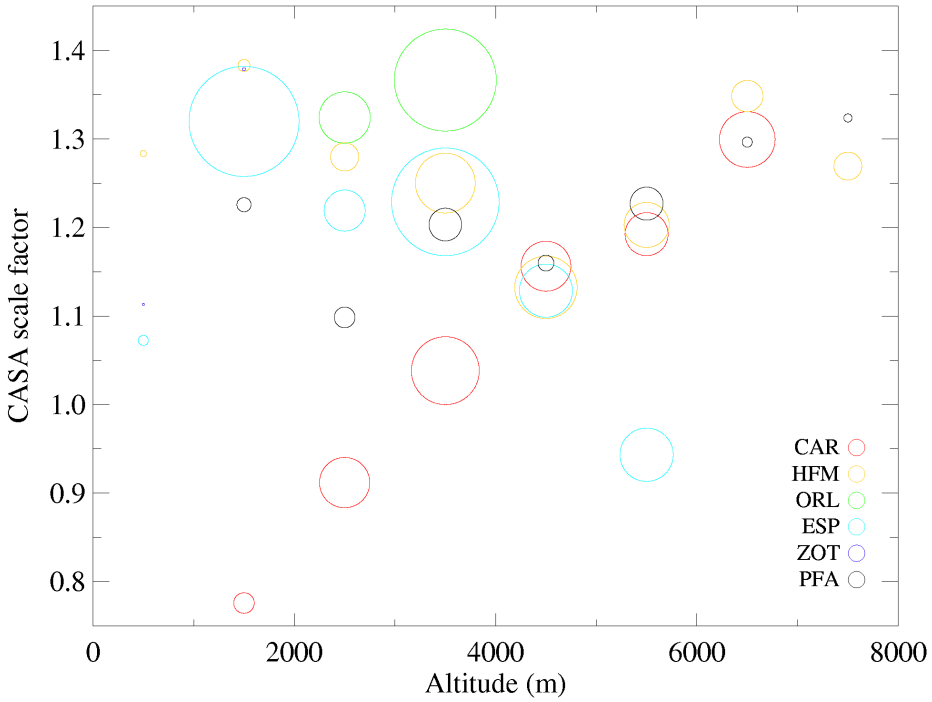

Figure 4.5: The optimized scale factors A for CASA terrestrial biosphere model fluxes required for minimizing the difference between the observations and simulations at different altitudes. The A values of 12 model-mean are given at each of the six aircraft sampling sites (marked by different colors). The radius of each circle is proportional to $1/\sigma^2$, where σ is the fit rms in ppmv.

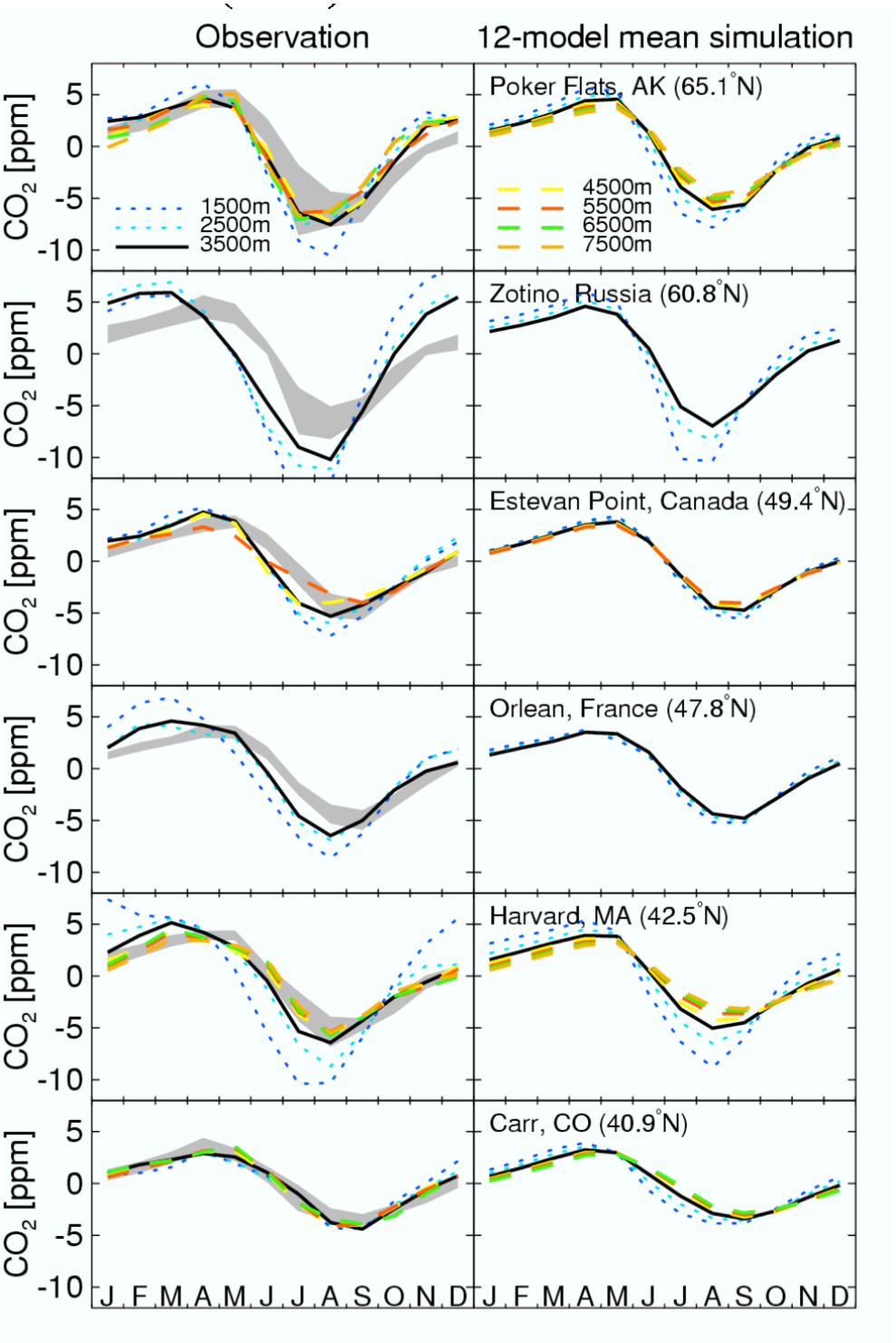

Figure 4.6: Comparison of the CO_2 seasonal cycles at different levels, for both the aircraft observations (left panel) and the TransCom 12-model mean simulation (right panel). Each altitude level is represented by a different line and each row represents one site respectively. The range of model simulations for 3500 meters altitude is also shown in the left panel as the shaded area.

4.5 Summary and implications

Comparison of the column-averaged CO_2 dry volume mixing ratio measurements and the TransCom models show that the CASA model underestimates the Northern Hemisphere growing season net fluxes by approximately 28%. Using multi-level observed CO_2 from the Northern hemisphere to diagnose the model performance at different altitudes, we identify substantial underestimation of free troposphere vertical mixing rates by TransCom models. While the mixing between the PBL and the free troposphere has been a major focus of carbon flux inversion experiments (i.e. TransCom), this analysis suggests that equally large errors exist in the rate of vertical mixing throughout the free troposphere.

Table 4.4: The optimal values of (a) scale factor, A_H and (b) time delay in days, T_H applied to 3500-m-level seasonal CO_2 change for best matching the other levels (Equation 4.3). For each site, the left column is for the observations and the right column is for the 12-model mean simulations.

	PFA		ZOT		ESP		ORL		HFM		CAR	
(a)	Optimal values for scale factor A_H											
Altitude	Obs	Mod.	Obs.	Mod.	Obs.	Mod.	Obs.	Mod.	Obs.	Mod.	Obs.	Mod.
7500m	0.88	0.80							0.78	0.74		
6500m	0.93	0.85							0.87	0.78	1.05	0.90
5500m	0.89	0.90			0.74	0.91			0.83	0.84	1.00	0.94
4500m	0.92	0.95			0.89	0.95			0.85	0.91	1.05	0.98
3500m	1.00	1.00	1.00	1.00	1.00	1.00	1.00	1.00	1.00	1.00	1.00	1.00
2500m	1.03	1.12	1.18	1.20	1.07	1.07	1.03	1.06	1.25	1.23	0.98	1.12
1500m	1.33	1.30	1.32	1.51	1.24	1.16	1.41	1.12	1.67	1.57	0.96	1.26
(b)	Optimal values for time delay T_H (days)											
Altitude	Obs.	Mod.	Obs.	Mod.	Obs.	Mod.	Obs.	Mod.	Obs.	Mod.	Obs.	Mod.
7500m	-2.0	7.0							13.0	13.0		
6500m	-4.0	6.0							11.0	10.0	3.0	12.0
5500m	-1.0	4.0			8.0	1.0			10.0	8.0	-2.0	10.0
4500m	0.0	2.0			-3.0	1.0			6.0	4.0	-4.0	8.0
3500m	0.0	0.0	0.0	0.0	0.0	0.0	0.0	0.0	0.0	0.0	0.0	0.0
2500m	-5.0	-4.0	-4.0	-5.0	-4.0	-1.0	-5.0	-3.0	-6.0	-6.0	-4.0	-8.0
1500m	-7.0	-10.0	-10.0	-10.0	-4.0	-2.0	-12.0	-7.0	-21.0	-13.0	-4.0	-16.0

The weak vertical exchange of the TransCom models will have impacts beyond the estimation of NEE. have shown, for example, that the inferred uptake of fossil fuel carbon by land in the

Northern Hemisphere by the various TransCom models (from 0.0 to 4.0 Pg C/yr depending on which transport model is used) is correlated with their estimate of the CO_2 seasonal cycle produced by the biosphere fluxes. *Gurney et al.* [2004] suggest that this correlation is consistent with errors in parameterization of the seasonal mixing efficiency between the *planetary boundary layer* and the *free troposphere*, which co-varies in time with the surface carbon exchange direction and strength [*Denning et al.*, 1995]. Our finding suggests that as a group, the TransCom models may have too little vertical mixing and so may overestimate the size of the Northern Hemisphere land sink. The validity of this inference, however, depends in part on the how the transport errors vary seasonally - something this study has not addressed.

The analysis described in this letter illustrates the utility of having information about the vertical distribution of CO_2 from aircraft. In addition, the total column measurements allow a more continuous record of CO_2 mass. The Total Carbon Column Observing Network (TCCON) is being established to expand the number of sites where CO_2 columns are measured (data available at `www.tccon.caltech.edu`). TCCON will include a number of sites in both the Northern and Southern Hemispheres. These observations should provide an improved measure of the gradient in CO_2 mass between the Hemispheres. Based on the findings of this study, we expect that the North-South gradient will be larger than predicted by the TransCom inversions tied to surface observations.

Chapter 5

The future of global carbon budget observation system

The key of carbon cycle research, at this time, is data collection of all forms. The Earth is a complicated system, and it will be naive to assume we can understand it with a few observation sites. The proposed methods listed in this chapter will be a good start.

5.1 Total Carbon Column Observing Network (TCCON)

The studies in previous three chapters have led to the creation of TCCON. This network includes existing and proposed ground-based Fourier Transform Spectrometers carefully selected to provide global coverage (see Figure 5.1 and Table 5.1). These spectrometers record direct solar spectra in the near-infrared spectral region, from which accurate column-averaged abundance of CO_2, CH_4, N_2O, HF, CO, H_2O, and HDO are retrieved. The network puts measuring carbon dioxide a priority to provide an essential validation resource for the coming CO_2 observing satellites.

Since 2004, several operational TCCON sites have achieved high precision for carbon dioxide measurements [*Warneke et al.*, 2005; *Washenfelder et al.*, 2006]. Initial efforts have also been made to use TCCON data to calibrate space-born CO_2 measurements [*Bösch et al.*, 2006; *Barkley et al.*, 2007].

Table 5.1: The detail information of TCCON sites and partners

Site Name	Location	Instrument	Status	Operator
Park Falls, Wisconsin	40°N, 90°W	Bruker 125HR	Operational 7/2004	California Institute of Technology
Lauder, New Zealand	45°S, 170°E	Bruker 120HR		National Institute of Water and Atmosphere Research, New Zealand
Bremen, Germany	53°N, 8°E	Bruker 125HR		University of Bremen
Ny Alesund, Norway	79°N, 11°E	Bruker 120HR	Operational 2/2002	University of Bremen, Alfred Wegener Institute
Darwin, Australia	12°S, 130°E	Bruker 125HR	Operational 9/2005	University of Wollongong
Wollongong, Australia	34°S, 151°E		Operational 1/2007	University of Wollongong
Lamont, Oklahoma	37°N, 98°W	Bruker 125HR	Expected to be operational 8/2008	California Institute of Technology
Izana, Tenerife	28°N, 16°W		Expected to be operational 2007	Institute of Meteorology and Climate Research, Forschungszentrum Karlsruhe and Univ. Karlsruhe
Garmisch, Germany	47°N, 11°E			
Bialystock, Poland	53°N, 22°E		Expected to be operational 8/2008	University of Bremen
Orleans, France	48°N, 2°E		Expected to be operational 8/2008	University of Bremen
Eureka, Canada	80°N, 85°W		Possible site	University of Toronto
Ascension Island	8°S, 14°W		Possible site	Max-Planck-Institut fur Biogeochemie

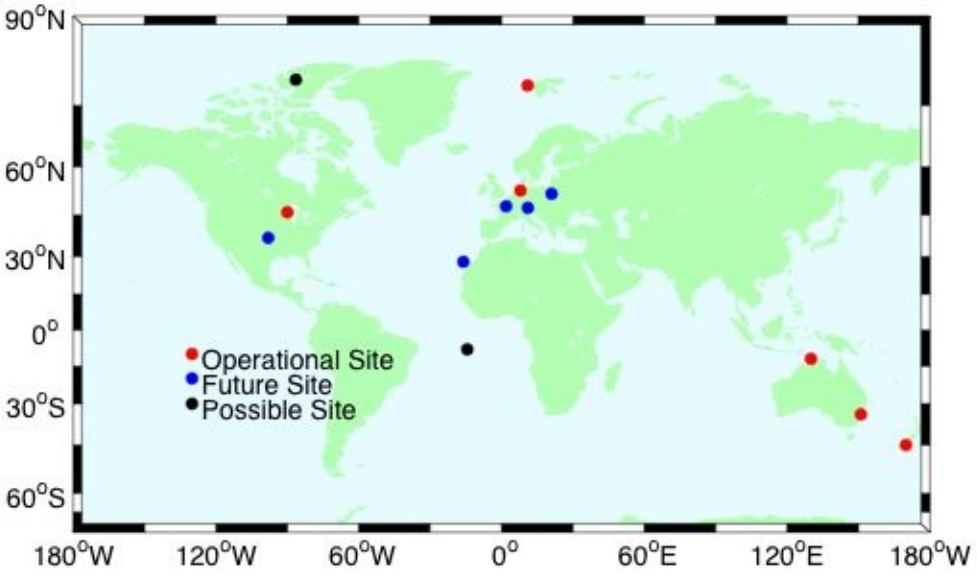

Figure 5.1: The locations of spectrometers of TCCON. The red dots are sites already in operation before 2007.

5.2 CO_2 observing satellites

The first space-borne observations were made by Japanese Interferometric Monitor for Greenhouse gases (IMG) [*Kobayashi et al.*, 1999a,b] aboard the Advance Earth Observing Satellite (ADEOS) launched on August 1996, although it only lasted eight months. Later studies have demonstrated the feasibility of observing carbon dioxide from space by reanalyzing infrared soundings from launched satellites, including HIRS-2[1] on the NOAA polar meteorological satellite [*Chédin et al.*, 2003a,b] and AIRS[2] on the NASA Aqua platform [*Crevoisier et al.*, 2004; *Chevallier et al.*, 2005; *Engelen and McNally*, 2005; *Chahine et al.*, 2005]. More recent studies by *Buchwitz et al.* [2005]; *Bösch et al.* [2006]; *Buchwitz et al.* [2007]; *Barkley et al.* [2007] used near IR spectra from the Scanning Imaging Absorption Spectrometer for Atmospheric Cartography (SCIAMACHY) on ENVISAT [*Burrows et al.*, 1995; *Bovensmann et al.*, 1999]. All these efforts have led to the development of the new generation high-precision (<0.3%) CO_2-dedicated satellites: OCO and GOSAT.

[1] High-Resolution Infrared Radiation Sounder
[2] Atmospheric Infra-Red Sounder

The Orbiting Carbon Observatory (OCO) [*Crisp et al.*, 2004] is a mission led by the Jet Propulsion Laboratory and sponsored by NASA's Earth System Science Pathfinder (ESSP) program. The Greenhouse gases Observing Satellite (GOSAT) [*Masahiro and Takashi*, 2005] is a joint project of Japan Aerospace Exploration Agency (JAXA), the Ministry of the Environment, and the National Institute for Environmental Studies (NIES). The two missions will have similar performance and orbit characters. Both satellites measure X_{CO_2} by using specially designed spectrometers to take solar reflection spectra from the Earth, although the spectrometers are of different type. OCO carries a 3-band (0.76 μm, 1.58 μm, 2.06 μm) grating spectrometer, and GOSAT carries a Fourier Transform Spectrometer [*Hamazaki et al.*, 2004, 2005] to take spectra between 1.56μm to 1.81 μm. After their launch in 2008, we hope to see great improvement of CO2 measurements coverage, which will enable the inversion of carbon fluxes at continental spatial resolution [*Rayner and O'Brien*, 2001].

5.3 Differential Absorption Lidar (DIAL)

Lidar (or Laser detection and ranging) is a remote sensing technology that measures properties of scattered light to find distance and other information of remote targets. It is an active detection technology: *i.e.* it uses its own light source instead of sun light or other nature light sources. This enables a lidar to operate during the nights and bad weather conditions, when passive observations are not available due to absence of natural light.

Using lidar to observe water vapor profiles dates back to the 1960s [*Schotland*, 1966]. Studies on observing other atmospheric trace gases including CO_2 started shortly after [*Reid et al.*, 1978; *Bufton et al.*, 1983; *Sugimoto and Minato*, 1993]. The principle is to use laser light pulses at different wavelengths at both the peak (on-line) and the wings (off-line) of an absorption band for the targeting molecular, then compare the back-scattering difference of on-line and off-line wavelengths to derive the molecular numbers along the light paths (shown in Figure 5.2). The

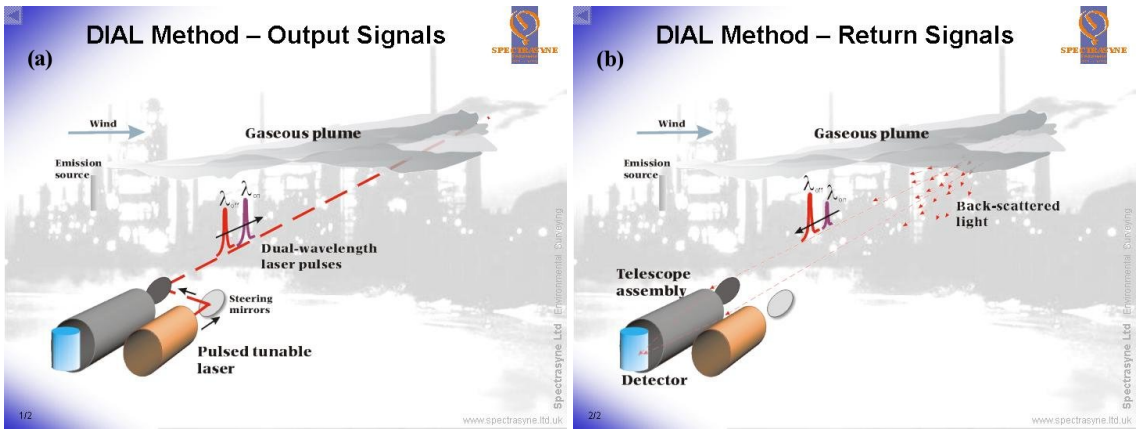

Figure 5.2: Principle of DIAL: (a) Two pulses with on-line wavelength λ_{on} and off-line wavelength λ_{off} are sent out by tunable laser into the atmosphere; (b) Small amount of light at on-line wavelength λ_{on} and off-line wavelength λ_{off} is back-scattered, collected by telescope assembly, and monitored by a detector. Figures are from *Spectrasyne Inc.* (`www.spectrasyne.ltd.uk`) with permission.

technology, termed as differential absorption Lidar (DIAL), was used first in ground-based observatories (e.g. [*Schotland*, 1966; *Reid et al.*, 1978]). Air-borne DIAL systems appeared in the late 1970s to early 1980s with developments at the Jet Propulsion Laboratory [*Shumate et al.*, 1981] and the NASA Langley Research Center [*Browell et al.*, 1983]. An experimental space-borne mission (lidar in-space technology experiment, or LITE) was also deployed by the space shuttle Discovery in September 1994 [*Browell et al.*, 1998].

Recently efforts in DIAL atmospheric CO_2 measurement by *Koch et al.* [2004]; *Gibert et al.* [2006] have achieved precision of 1~2% from the ground, which is larger than the 0.3% accuracy generally required by global carbon cycle research [*Rayner and O'Brien*, 2001]. New laser source with high energy and stability (e.g. Fiber laser used by [*Abshire et al.*, 2006]) may significantly improve the situation and provide another independent method for measuring CO_2 from the ground and space.

5.4 Unmanned Aerial Vehicle (UAV)

Airborne carbon dioxide sampling missions (e.g. *Levin et al.* [2002]; *Tans* [2007a]) have provided important information about the temporal and spatial variation of atmosphere CO_2, especially for modeling the vertical mixing "rectifier effect"[*Denning et al.*, 1999]. However, the number of these missions are limited by the high cost of piloted aircraft: the rental for a single-engine piston plane is $75/hr to $115/hr, or double that once insurance and pilot wage are added. Thus CO_2 profiles are only taken once every 5-10 days at Briggsdale, Colorado and every three weeks at Zotino, Russia (see the site description of *GlobalView-CO_2* [2006]).

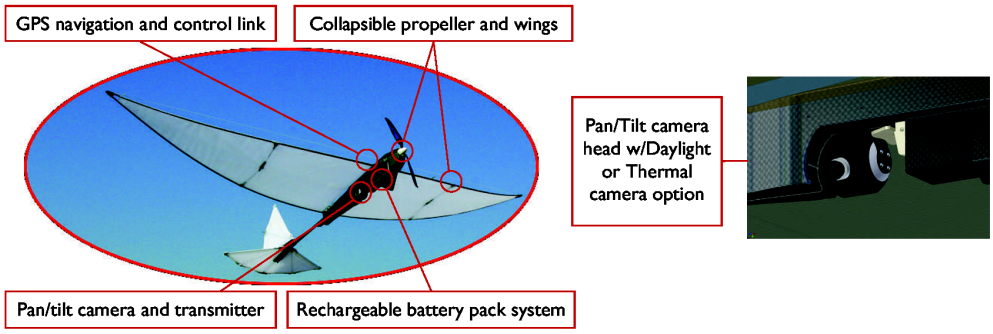

Operating specifications

Wing span:	6.5 feet (1.98 meters)
Total weight:	4 lbs (1.81 kg)
Endurance:	~ 70 minutes with rechargeable Lithium Polymer battery
Speed:	21 knots max: 24 knots min: 16 knots
Range:	2 miles LOS (3.2 km) (extensible via Octatron NetWeaver™)
Propulsion:	Tractor-drive electric folding propeller
Pan/tilt:	350° pan and 90° tilt

Figure 5.3: Design and Specifications of Octatron SkySeer^{TM}[*Product brochure, Octatron Inc.*]

The Unmanned Aerial Vehicle (UAV) is a much more economical and flexible alternative to manned aircraft. Several recent studies [*Sherwood*, 2005; *Fladeland et al.*, 2005; *Watai et al.*, 2006] have demonstrated the possibility of constructing a low-cost, low-maintenance UAV system specifically for atmosphere CO_2 sampling. A good example is *Watai et al.* [2006], who have devel-

oped a lightweight (~3.5 kg) CO_2 observation system with a precision of ± 0.26 ppm, which can be installed on a small UAV (Kite Plane, Sky Remote, Japan). The UAV is autonomously navigated by a GPS system, with a ceiling altitude of 3000 m and endurance of 1.5 hours. The U.S. Octatron SkySeer^{TM}(See Figure 5.3) provides similar performance with total cost of $25,000 to $30,000. These type of UAVs, together with the effort on cheap ($2000 per device) UAV-borne atmosphere CO_2 sensor, such as the one supported by U.S. Department of Energy [*Dahlman and Goswami*, 2005], will enable most carbon cycle researchers to get frequent CO_2 profiles in vast regions of interest with minimal expense in the near future.

5.5 Passenger aircraft

The idea of using passenger aircraft to provide regular atmospheric trace gases measurements along major airline routes started in the 1990s, when JAL Foundation (`www.jal-foundation.or.jp`) began to support a study to collect air samples in flights between Japan and Australia using a Boeing 747 [*Matsueda and Inoue*, 1996]. The main advantage is that it can provide near-global coverage and high sampling rate with modest cost, even compared with ground-based observation system. The passenger aircrafts are therefore referred sometimes as "the poor man's satellite" [*Brenninkmeijer et al.*, 2005].

Atmospheric CO_2 measurements were included in the initial effort of JAL project [*Matsueda and Inoue*, 1996; *Matsueda et al.*, 2002], which has since expanded from one to seven aircrafts that cover large area of (Figure 5.4) Pacific and Eurasia. Another effort on passenger aircraft CO_2 measurements is included in the European CARIBIC (Civil Aircraft for the Regular Investigation of the Atmosphere Based on an Instrument Container) project [*Brenninkmeijer et al.*, 1999; *Zimmermann et al.*, 2002; *Brenninkmeijer et al.*, 2005, 2007]. Since all passenger aircrafts are able to carry the payload of a UAV-based CO_2 sensor, it will be a fast and low-cost way to expand the global carbon dioxide measurements inside the upper troposphere and lower stratosphere.

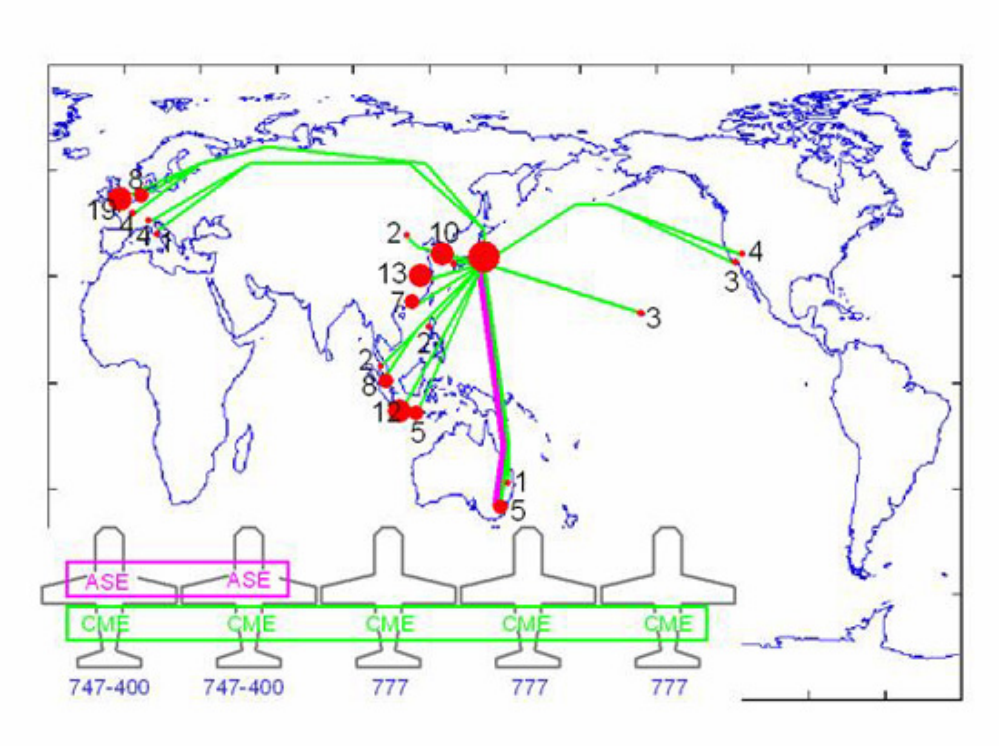

Figure 5.4: JAL passenger aircraft CO_2 sampling network in 2006. Red dots are flight destinations with numbers showing the monthly sample rates. Green lines (CME or Carbon dioxide Measuring Equipment) are routes with only CO_2 measurements, and the cyan line (ASE or Air Sampling Equipment) is the route with air sample collections. (Figure from *Machida* [2005])

5.6 Perspectives

Carbon is the “element of life”, so global carbon cycle research carries more important goals than the study of global warming. My hope is that all my researches can eventually lead to insights of interactions among all terrestrial living species, from single-cell algae to complex *homo sapiens*. To me, the knowledge of carbon cycle can be keys to a better future, where human beings can conduct responsibly on a planet that is not only occupied by our kind but also by all forms of other lives.

Bibliography

Abshire, J. B., et al. (2006), Laser Sounder for Global Measurement of CO_2 concentrations in the Troposphere from Space (a progress report), in *2006 Earth Science Technology Conference, University of Maryland, College Park, MD*.

Adams, R. M., et al. (1990), Global climate change and united-states agriculture, *Nature*, *345*, 219–224, 31.

Andres, R. J., G. Marland, I. Fung, and E. Matthews (1996), A 1 degrees $\times$ 1 degrees distribution of carbon dioxide emissions from fossil fuel consumption and cement manufacture, 1950-1990, *Global Biogeochemical Cycles*, *10*, 419–429.

Andres, R. J., D. J. Fielding, G. Marland, T. A. Boden, N. Kumar, and A. T. Kearney (1999), Carbon dioxide emissions from fossil-fuel use, 1751-1950, *Tellus Series B - Chemical and Physical Meteorology*, *51*, 759–765, 18.

Asano, S., M. Shiobara, and A. Uchiyama (1995), Estimation of cloud physical parameters from airborne solar spectral reflectance measurements for stratocumulus clouds, *Journal of Atmospheric Science*, *52*, 3556–3576.

Aubinet, M. (2000), Estimates of the annual net carbon and water exchange of forests: The EUROFLUX methodology, *Advances in Ecological Research*, *30*, 113–176.

Baker, D. F., et al. (2006), TransCom 3 inversion intercomparison: Impact of transport model errors on the interannual variability of regional CO_2 fluxes, 1988-2003, *Global Biogeochemical Cycles*, *20*.

Baldocchi, D., R. Valentini, S. Running, W. Oechel, and R. Dahlman (1996), Strategies for measuring and modelling carbon dioxide and water vapour fluxes over terrestrial ecosystems, *Global Change Biology*, *2*, 159–168.

Baldocchi, D., et al. (2001), Fluxnet: A new tool to study the temporal and spatial variability of ecosystem-scale carbon dioxide, water vapor, and energy flux densities, *Bulletin of the American Meteorological Society*, *82*, 2415–2434.

Baldocchi, D., et al. (2006), FLUXNET: A Global Network Measuring and Assessing Spatial-Temporal Variability of Carbon Dioxide, Water Vapor and Energy Fluxes between the Terrestrial Biosphere and Atmosphere, *Tech. Rep. NSF 06-567*, National Science Foundation Research Coordination Networks in Biological Sciences.

Baldocchi, D. D., B. B. Hincks, and T. P. Meyers (1988), Measuring Biosphere-Atmosphere Exchanges of Biologically Related Gases with Micrometeorological Methods, *Ecology*, *69*, 1331–1340.

Barkley, M. P., et al. (2007), Assessing the near surface sensitivity of SCIAMACHY atmospheric CO_2 retrieved using (FSI) WFM-DOAS, *Atmospheric Chemistry and Physics*, *7*, 3597–3619.

Barnola, J. M., D. Raynaud, Y. S. Korotkevich, and C. Lorius (1987), Vostok ice core provides 160,000-year record of atmospheric CO_2, *Nature*, *329*, 408–414, 43.

Battle, M., M. L. Bender, P. P. Tans, J. W. C. White, J. T. Ellis, T. Conway, and R. J. Francey (2000), Global carbon sinks and their variability inferred from atmospheric O_2 and δ^{13}C, *Science*, *287*, 2467–2470.

Bender, M., T. Ellis, P. Tans, R. Francey, and D. Lowe (1996), Variability in the O_2/N_2 ratio of southern hemisphere air, 1991-1994: Implications for the carbon cycle, *Global Biogeochemical Cycles*, *10*, 9–21, 26.

Bentamy, A., K. B. Katsaros, A. M. Mestas-Nuñez, W. M. Drennan, E. B. Forde, and H. Roquet (2003), Satellite estimates of wind speed and latent heat flux over the global oceans, *Journal of Climate*, *16*, 637–656.

Bösch, H., et al. (2006), Space-based Near-Infrared CO_2 measurements: Testing the Orbiting Carbon Observatory Retrieval Algorithm and Validation Concept using SCIAMACHY Observations over Park Falls, Wisconsin, *Journal of Geophysical Research*, *111*(D23302), doi: 10.1029/2006JD007080.

Bousquet, P., P. Peylin, P. Ciais, C. L. Quere, P. Friedlingstein, and P. P. Tans (2000), Regional changes in carbon dioxide fluxes of land and oceans since 1980, *Science*, *290*, 1342–1346.

Bovensmann, H., J. P. Burrows, M. Buchwitz, J. Frerick, S. Noël, V. V. Rozanov, K. V. Chance, and A. P. H. Goede (1999), Sciamachy: Mission Objectives and Measurement Modes, *Journal of the Atmospheric Sciences*, *56*, 127–150.

Brenninkmeijer, C. A. M., F. Slemr, C. Koeppel, and D. Scharffe (2005), Analyzing atmospheric trace gases and aerosols using passenger aircraft, *EOS*, *86*, 77–88.

Brenninkmeijer, C. A. M., et al. (1999), CARIBIC – Civil Aircraft for Global Measurement of Trace Gases and Aerosols in the Tropopause Region, *Journal of Atmospheric and Oceanic Technology*, *16*, 1373–1383.

Brenninkmeijer, C. A. M., et al. (2007), Civil aircraft for the regular investigation of the atmosphere based on an instrumented container: The new CARIBIC system, *Atmospheric Chemistry and Physics*, *7*, 4953–4976.

Browell, E. V., A. F. Carter, S. T. Shipley, R. J. Allen, C. F. Butler, M. N. Mayo, J. H. Siviter, Jr, and W. M. Hall (1983), NASA multipurpose airborne DIAL system and measurements of ozone and aerosol profiles, *Applied Optics*, *22*, 522.

Browell, E. V., S. Ismail, and W. B. Grant (1998), Differential absorption lidar (DIAL) measurements from air and space, *Applied Physics B: Lasers and Optics*, *67*, 399–410.

Brown, L. R., and C. Plymate (2000), Experimental line parameters of the oxygen A-band at 760 nm, *Journal of Molecular Spectroscopy*, *199*, 166–179.

Buchwitz, M., O. Schniesing, J. P. Burrows, H. Bovensmann, M. Reuter, and J. Notholt (2007), First direct observation of the atmospheric CO_2 year-to-year increase from space, *Atmospheric Chemistry and Physics*, *7*, 4249–4256.

Buchwitz, M., et al. (2005), Atmospheric methane and carbon dioxide from SCIAMACHY satellite data: initial comparison with chemistry and transport models, *Atmospheric Chemistry and Physics*, *5*, 941–962.

Bufton, J. L., T. Itabe, L. L. Strow, C. L. Korb, B. M. Gentry, and C. Y. Weng (1983), Frequency-doubled CO_2 lidar measurement and diode laser spectroscopy of atmospheric CO_2, *Applied Optics*, *22*, 2592.

Burrows, J. P., E. Holzle, A. P. H. Goede, H. Visser, and W. Fricke (1995), SCIAMACHY–scanning imaging absorption spectrometer for atmospheric chartography, *Acta Astronautica*, *35*, 445–451.

Cageao, R. P., J. F. Blavier, J. P. McGuire, Y. B. Jiang, V. Nemtchinov, F. P. Mills, and S. P. Sander (2001), High-resolution fourier-transform ultraviolet-visible spectrometer for the measurement of atmospheric trace species: application to OH, *Applied Optics*, *40*, 2024–2030.

Chahine, M., C. Barnet, E. T. Olsen, L. Chen, and E. Maddy (2005), On the determination of atmospheric minor gases by the method of vanishing partial derivatives with application to CO_2, *Geophysical Research Letters*, *32*, L22,803, doi:10.1029/2005GL024165.

Chédin, A., R. Saunders, A. Hollingsworth, N. Scott, M. Matricardi, J. Etcheto, C. Clerbaux,

R. Armante, and C. Crevoisier (2003a), The feasibility of monitoring CO_2 from high-resolution infrared sounders, *Journal of Geophysical Research*, *108*, 4064, doi:10.1029/2001JD001443.

Chédin, A., S. Serrar, N. A. Scott, C. Crevoisier, and R. Armante (2003b), First global measurement of midtropospheric CO_2 from NOAA polar satellites: Tropical zone, *Journal of Geophysical Research*, *108*, 4581, doi:10.1029/2003JD003439.

Chevallier, F., R. J. Engelen, and P. Peylin (2005), The contribution of AIRS data to the estimation of CO_2 sources and sinks, *Geophysical Research Letters*, *32*, 4.

Chevallier, F., F. M. Breon, and P. J. Rayner (2007), Contribution of the orbiting carbon observatory to the estimation of CO_2 sources and sinks: Theoretical study in a variational data assimilation framework, *Journal of Geophysical Research-Atmospheres*, *112*, 11.

Ciais, P., P. P. Tans, M. Trolier, J. W. C. White, and R. J. Francey (1995a), A large northern-hemisphere terrestrial CO_2 sink indicated by the $^{13}C/^{12}C$ ratio of atmospheric CO_2, *Science*, *269*, 1098–1102, 29.

Ciais, P., et al. (1995b), Partitioning of ocean and land uptake of CO_2 as inferred by $\delta^{13}c$ measurements from the NOAA climate monitoring and diagnostics laboratory global air sampling network, *Journal of Geophysical Research-Atmospheres*, *100*, 5051–5070, 98.

Clough, S. A., F. X. Kneizys, and R. W. Davies (1989), Line shape and the water vapor continuum, *Atmospheric Research*, *23*, 229–241.

Corfee-Morlot, J., and N. Hohne (2003), Climate change: long-term targets and short-term commitments, *Global Environmental Change-Human and Policy Dimensions*, *13*, 277–293.

Crevoisier, C., S. Heilliette, A. Chédin, S. Serrar, R. Armante, and N. A. Scott (2004), Midtropospheric CO_2 concentration retrieval from AIRS observations in the Tropics, *Geophysical Research Letters*, *31*, L17,106, doi:10.1029/2004GL020141.

Crisp, D., et al. (2004), *The orbiting carbon observatory (OCO) mission*, *Advances in Space Research*, vol. 34, pp. 700–709, Pergamon-Elsevier Science Ltd, Kidlington.

Dahlman, R., and K. Goswami (2005), Long-Term, Autonomous Measurement of Atmospheric Carbon Dioxide Using an Ormosil-Nanocomposite-Based Optical Sensor. (Final Report, July 13, 2004 - April 12, 2005), *Final Technical Progress Report DE2006-875422*, InnoSense LLC, Lomita, CA, USA, available at Department of Energy Information Bridge and National Technical Information Service.

Denning, A. S., I. Y. Fung, and D. Randall (1995), Latitudinal gradient of atmospheric CO_2 due to seasonal exchange with land biota, *Nature*, *376*, 240–243.

Denning, A. S., T. Takahashi, and P. Friedlingstein (1999), Can a strong atmospheric CO_2 rectifier effect be reconciled with a ¨reasonable¨ carbon budget?, *Tellus Series B - Chemical and Physical Meteorology*, *51*, 249–253.

Dickinson, R. E., and R. J. Cicerone (1986), Future global warming from atmospheric trace gases, *Nature*, *319*, 109–115.

Dixon, R. K., S. Brown, R. A. Houghton, A. M. Solomon, M. C. Trexler, and J. Wisniewski (1994), Carbon pools and flux of global forest ecosystems, *Science*, *263*, 185–190.

Eamus, D., and P. G. Jarvis (1989), The direct effects of increase in the global atmospheric CO_2 concentration on natural and commercial temperate trees and forests, *Advances in Ecological Research*, *19*, 1–55.

Emanuel, K. (2005), Increasing destructiveness of tropical cyclones over the past 30 years, *Nature*, *436*, 686–688.

Emanuel, K. A. (1987), The dependence of hurricane intensity on climate, *Nature*, *326*, 483–485.

Engelen, R. J., and A. P. McNally (2005), Estimating atmospheric CO_2 from advanced infrared satellite radiances within an operational four-dimensional variational (4D-Var) data assimilation

system: Results and validation, *Journal of Geophysical Research, 110*(D18305), doi:10.1029/2005JD005982.

Enting, I. G., C. M. Trudinger, and R. J. Francey (1995), A Synthesis Inversion of the Concentration and δ^{13}C of Atmospheric CO_2, *Tellus Series B - Chemical and Physical Meteorology*, *47*, 35–52.

Fan, S., M. Gloor, J. Mahlman, S. Pacala, J. Sarmiento, T. Takahashi, and P. Tans (1998), A large terrestrial carbon sink in North America implied by atmospheric and oceanic carbon dioxide data and models, *Science*, *282*, 442–446, 46.

Fang, J., A. Chen, C. Peng, S. Zhao, and L. Ci (2001), Changes in forest biomass carbon storage in China between 1949 and 1998, *Science*, *292*, 2320–2322.

Fladeland, M., D. Sullivan, R. Dobosy, and T. Takahashi (2005), A suborbital observation system for measuring carbon flux over land and water, in *Advancing Contemporary Aerospace Technologies and Their Integration*, pp. 1–10, American Institute of Aeronautics and Astronautics, Arlington, VA.

Gamache, R. R., A. Goldman, and L. S. Rothman (1998), Improved spectral parameters for the three most abundant isotopomers of the oxygen molecule, *Journal of Quantitative Spectroscopy & Radiative Transfer*, *59*, 495–509.

Gibert, F., P. Flamant, D. Bruneau, and C. Loth (2006), Two-micrometer heterodyne differential absorption lidar measurements of the atmospheric CO_2 mixing ratio in the boundary layer, *Applied Optics*, *45*, 4448–4458.

GlobalView-CO_2 (2006), Cooperative Atmosphere Data Integration Project - Carbon Dioxide. CD-ROM, [Also available on Internet via anonymous FTP to ftp.cmdl.noaa.gov, Path: ccg/co2/GLOBALVIEW].

Gloor, M., S. M. Fan, S. Pacala, and J. Sarmiento (2000), Optimal sampling of the atmosphere for purpose of inverse modeling: A model study, *Global Biogeochemical Cycles*, *14*, 407–428.

Goldenberg, S. B., C. W. Landsea, A. M. Mestas-Nunez, and W. M. Gray (2001), The recent increase in atlantic hurricane activity: Causes and implications, *Science*, *293*, 474–479, 43.

Gruber, N., J. L. Sarmiento, and T. F. Stocker (1996), An improved method for detecting anthropogenic CO_2 in the oceans, *Global Biogeochemical Cycles*, *10*, 809–837, 95.

Gurney, K. R., et al. (2002), Towards robust regional estimates of CO_2 sources and sinks using atmospheric transport models, *Nature*, *415*, 626–630.

Gurney, K. R., et al. (2003), TransCom 3 CO_2 inversion intercomparison: 1. annual mean control results and sensitivity to transport and prior flux information, *Tellus Series B - Chemical and Physical Meteorology*, *55*, 555–579.

Gurney, K. R., et al. (2004), TransCom 3 inversion intercomparison: Model mean results for the estimation of seasonal carbon sources and sinks, *Global Biogeochemical Cycles*, *18*.

HaDuong, M., M. J. Grubb, and J. C. Hourcade (1997), Influence of socioeconomic inertia and uncertainty on optimal CO_2-emission abatement, *Nature*, *390*, 270–273.

Hamazaki, T., A. Kuze, and K. Kondo (2004), Sensor system for Greenhouse Gas Observing Satellite (GOSAT), in *Infrared Spaceborne Remote Sensing XII. Edited by Strojnik, Marija. Proceedings of the SPIE*, vol. 5543, pp. 275–282.

Hamazaki, T., Y. Kaneko, A. Kuze, and K. Kondo (2005), Fourier transform spectrometer for Greenhouse Gases Observing Satellite (GOSAT), in *Enabling Sensor and Platform Technologies for Spaceborne Remote Sensing. Edited by Komar, George J.; Wang, Jinxue; Kimura, Toshiyoshi. Proceedings of the SPIE*, vol. 5659, pp. 73–80.

Hirono, M., and T. Nakazawa (1982), The shape of spectral lines with combined impact and statistical broadenings, *Journal of the Physical Society of Japan*, *51*, 265–268.

Houghton, R. A. (2003), Why are estimates of the terrestrial carbon balance so different?, *Global Change Biology*, *9*, 500–509.

Houghton, R. A., J. E. Hobbie, J. M. Melillo, B. Moore, B. J. Peterson, G. R. Shaver, and G. M. Woodwell (1983), Changes in the carbon content of terrestrial biota and soils between 1860 and 1980 - A net release of CO_2 to the atmosphere, *Ecological Monographs*, *53*, 235–262, 135.

Hsueh, D. Y., N. Y. Krakauer, J. T. Randerson, X. M. Xu, S. E. Trumbore, and J. R. Southon (2007), Regional patterns of radiocarbon and fossil fuel-derived CO_2 in surface air across North America, *Geophysical Research Letters*, *34*, 6.

Huang, N. E., Z. Shen, S. R. Long, M. L. C. Wu, H. H. Shih, Q. N. Zheng, N. C. Yen, C. C. Tung, and H. H. Liu (1998), The empirical mode decomposition and the hilbert spectrum for nonlinear and non-stationary time series analysis, *Proceedings of the Royal Society of London Series a-Mathematical Physical and Engineering Sciences*, *454*, 903–995.

IPCC (1995), Climate Change 1994: Radiative Forcing of Climate Change and An Evaluation of the IPCC IS92 Emission Scenarios.

IPCC (2001), Climate Change 2001, the Third Accessment Report (TAR).

IPCC (2007), Climate Change 2007, the Fourth Accessment Report (AR4).

Jarvis, P. G. (1989), Atmospheric carbon-dioxide and forests, *Philosophical Transactions of the Royal Society of London Series B-Biological Sciences*, *324*, 369–392, 63.

Kallbekken, S., and N. Rive (2007), Why delaying emission reductions is a gamble, *Climatic Change*, *82*, 27–45.

Kaminski, T., M. Heimann, and R. Giering (1999), A coarse grid three-dimensional global inverse model of the atmospheric transport - 2. Inversion of the transport of CO_2 in the 1980s, *Journal of Geophysical Research-Atmospheres*, *104*, 18,555–18,581.

Kauppi, P. E., K. Mielikainen, and K. Kuusela (1992), Biomass and carbon budget of european forests, 1971 to 1990, *Science*, *256*, 70–74.

Keeling, C. D. (1958), The concentration and isotopic abundances of atmospheric carbon dioxide in rural areas, *Geochimica Et Cosmochimica Acta*, *13*, 322–334, 16.

Keeling, C. D. (1961), The concentration and isotopic abundances of carbon dioxide in rural and marine air, *Geochimica Et Cosmochimica Acta*, *24*, 277–298.

Keeling, C. D., T. P. Whorf, M. Wahlen, and J. van der Plichtt (1995), Interannual extremes in the rate of rise of atmospheric carbon dioxide since 1980, *Nature*, *375*, 666–670.

Keeling, R. F., and S. R. Shertz (1992), Seasonal and interannual variations in atmospheric oxygen and implications for the global carbon-cycle, *Nature*, *358*, 723–727, 25.

Keeling, R. F., S. C. Piper, and M. Heimann (1996), Global and hemispheric CO_2 sinks deduced from changes in atmospheric O_2 concentration, *Nature*, *381*, 218–221, 34.

Knutson, T. R., and R. E. Tuleya (2004), Impact of CO_2-induced warming on simulated hurricane intensity and precipitation: Sensitivity to the choice of climate model and convective parameterization, *Journal of Climate*, *17*, 3477–3495, 62.

Kobayashi, H., A. Shimota, K. Kondo, E. Okumura, Y. Kameda, H. Shimoda, and T. Ogawa (1999a), Development and evaluation of the interferometric monitor for greenhouse gases: a high-throughput Fourier-transform infrared radiometer for nadir earth observation, *Applied Optics*, *38*, 6801–6807.

Kobayashi, H., A. Shimota, C. Yoshigahara, I. Yoshida, Y. Uehara, and K. Kondo (1999b), Satellite-borne high-resolution FTIR for lower atmosphere sounding and its evaluation, *IEEE Transactions on Geoscience and Remote Sensing*, *37*, 1496–1507.

Koch, G. J., et al. (2004), Coherent differential absorption lidar measurements of CO_2, *Applied Optics*, *43*, 5092–5099.

Krakauer, N. Y., T. Schneider, J. T. Randerson, and S. C. Olsen (2004), Using generalized cross-validation to select parameters in inversions for regional carbon fluxes, *Geophysical Research Letters, 31*.

Kristensen, L. K. (1998), Astronomical refraction and airmass, *Astronomische Nachrichten*, *319*, 193–198.

Kuang, Z. M., J. Margolis, G. Toon, D. Crisp, and Y. Yung (2002), Spaceborne measurements of atmospheric CO_2 by high-resolution NIR spectrometry of reflected sunlight: An introductory study, *Geophysical Research Letters*, *29*, art. no.–1716.

Kurz, W. A., and M. J. Apps (1999), A 70-year retrospective analysis of carbon fluxes in the Canadian forest sector, *Ecological Applications*, *9*, 526–547.

Kuze, A., and K. V. Chance (1994), Analysis of Cloud-Top Height and Cloud Coverage from Satellites Using the O_2 A-band and B-bands, *Journal of Geophysical Research-Atmospheres*, *99*, 14,481–14,491.

Levin, I., and U. Karstens (2007), Inferring high-resolution fossil fuel CO_2 records at continental sites from combined $^{14}CO_2$ and CO observations, *Tellus Series B - Chemical and Physical Meteorology*, *59*, 245–250.

Levin, I., B. Kromer, M. Schmidt, and H. Sartorius (2003), A novel approach for independent budgeting of fossil fuel CO_2 over europe by $^{14}CO_2$ observations, *Geophysical Research Letters*, *30*, 5.

Levin, I., et al. (2002), Three years of trace gas observations over the EuroSiberian domain derived from aircraft sampling - A concerted action, *Tellus Series B - Chemical and Physical Meteorology*, *54*, 696–712.

Levitus, S., J. I. Antonov, T. P. Boyer, and C. Stephens (2000), Warming of the world ocean, *Science*, *287*, 2225–2229, 30.

Machida, T. (2005), Success in using regular civil aircraft to measure atmosphere CO_2. [www.env.go.jp/earth/nies_press/co2/index.html], online report in Japanese.

Marland, G., T. A. Boden, and R. J. Andres (2007), Global, Regional, and National Fossil Fuel CO_2 Emissions. In Trends: A Compendium of Data on Global Change.

Masahiro, K., and H. Takashi (2005), Overview of Greenhouse Gases Observing Satellite (GOSAT), *IEIC Technical Report (Institute of Electronics, Information and Communication Engineers)*, *104*, 49–53.

Matear, R. J., C. S. Wong, and L. Xie (2003), Can CFCs be used to determine anthropogenic CO_2?, *Global Biogeochemical Cycles*, *17*, 13, 24.

Matsueda, H., and H. Y. Inoue (1996), Measurements of atmospheric CO_2 and CH_4 using a commercial airliner from 1993 to 1994, *Atmospheric Environment*, *30*, 1647–1655.

Matsueda, H., H. Y. Inoue, and M. Ishii (2002), Aircraft observation of carbon dioxide at 8-13 km altitude over the western pacific from 1993 to 1999, *Tellus Series B - Chemical and Physical Meteorology*, *54*, 1–21.

Matsumoto, K., and N. Gruber (2005), How accurate is the estimation of anthropogenic carbon in the ocean? an evaluation of the Δ^*C method, *Global Biogeochemical Cycles*, *19*, 17, 43.

McGuire, A. D., et al. (2001), Carbon balance of the terrestrial biosphere in the twentieth century: Analyses of CO_2, climate and land use effects with four process-based ecosystem models, *Global Biogeochemical Cycles*, *15*, PAGES 183–206.

Meehl, G. A., W. M. Washington, W. D. Collins, J. M. Arblaster, A. X. Hu, L. E. Buja, W. G. Strand, and H. Y. Teng (2005), How much more global warming and sea level rise?, *Science*, *307*, 1769–1772.

Mendelsohn, R., W. D. Nordhaus, and D. Shaw (1994), The impact of global warming on agriculture – A Ricardian analysis, *American Economic Review*, *84*, 753–771, 17.

Min, Q., L. C. Harrison, and E. E. Clothiaux (2001), Joint statistics of photon path length and cloud optical depth: Case studies, *Journal of Geophysical Research-Atmospheres*, *106*, 7375–7385.

Mlawer, E. J., S. A. Clough, P. D. Brown, T. M. Stephen, J. C. Landry, A. Goldman, and F. J. Murcray (1998), Observed atmospheric collision-induced absorption in near-infrared oxygen bands, *Journal of Geophysical Research-Atmospheres*, *103*, 3859–3863.

Neftel, A., E. Moor, H. Oeschger, and B. Stauffer (1985), Evidence from polar ice cores for the increase in atmospheric CO_2 in the past 2 centuries, *Nature*, *315*, 45–47.

Newman, S. M., A. J. Orr-Ewing, D. A. Newnham, and J. Ballard (2000), Temperature and pressure dependence of line widths and integrated absorption intensities for the O_2 $a^1\Delta_g$-$X^3\Sigma_g^-$ (0,0) transition, *Journal of Physical Chemistry A*, *104*, 9467–9480.

Notholt, J., A. Meier, and S. Peil (1995), Total column densities of Tropospheric and Stratospheric trace gases in the undisturbed Arctic summer atmosphere, *Journal of Atmospheric Chemistry*, *20*, 311–332.

O'Brien, D. M., and R. M. Mitchell (1992), Error-Estimates for Retrieval of Cloud-Top Pressure Using Absorption in the A-band of Oxygen, *Journal of Applied Meteorology*, *31*, 1179–1192.

O'Brien, D. M., R. M. Mitchell, S. A. English, and G. A. D. Costa (1998), Airborne measurements of air mass from O_2 A-band absorption spectra, *Journal of Atmospheric and Oceanic Technology*, *15*, 1272–1286.

Olsen, S. C., and J. T. Randerson (2004), Differences between surface and column atmospheric CO_2 and implications for carbon cycle research, *Journal of Geophysical Research-Atmospheres*, *109*, 11.

Pougatchev, N. S., B. J. Connor, and C. P. Rinsland (1995), Infrared measurements of the Ozone vertical-distribution above Kitt Peak, *Journal of Geophysical Research-Atmospheres*, *100*, 16,689–16,697.

Randerson, J. T., M. V. Thompson, T. J. Conway, I. Y. Fung, and C. B. Field (1997), The contribution of terrestrial sources and sinks to trends in the seasonal cycle of atmospheric carbon dioxide, *Global Biogeochemical Cycles*, *11*, 535–560.

Rayner, P. J., and D. M. O'Brien (2001), The utility of remotely sensed CO_2 concentration data in surface source inversions, *Geophysical Research Letters*, *28*, 175–178.

Rayner, P. J., I. G. Enting, R. J. Francey, and R. Langenfelds (1999), Reconstructing the recent carbon cycle from atmospheric CO_2, $\delta^{13}C$ and O_2/N_2 observations, *Tellus Series B - Chemical and Physical Meteorology*, *51*, 213–232.

Reid, J., B. K. Garside, J. Shewchum, M. El-Sherbiny, and E. A. Ballik (1978), High sensitivity point monitoring of atmospheric gases employing tunable diode lasers, *Applied Optics*, *17*, 1806–1810.

Ritter, K. J., and T. D. Wilkerson (1987), High-Resolution Spectroscopy of the Oxygen A-Band, *Journal of Molecular Spectroscopy*, *121*, 1–19.

Rosenberg, N. J. (1981), The increasing CO_2 concentration in the atmosphere and its implication on agricultural productivity .1. Effects on photosynthesis, transpiration and water-use efficiency, *Climatic Change*, *3*, 265–279, 23.

Rothman, L. S., et al. (1998), The HITRAN molecular spectroscopic database and HAWKS (HITRAN Atmospheric Workstation): 1996 edition, *Journal of Quantitative Spectroscopy and Radiative Transfer*, *60*, 665–710, 291.

Sabine, C. L., et al. (2002), Distribution of anthropogenic CO_2 in the Pacific Ocean, *Global Biogeochemical Cycles*, *16*, 17.

Schlesinger, W. H. (1984), *Soil organic matter: A source of atmospheric CO_2*, pp. 111–127, Wiley, New York.

Schneider, M., F. Hase, and T. Blumenstock (2006), Ground-based remote sensing of HDO/H_2O ratio profiles: introduction and validation of an innovative retrieval approach, *Atmospheric Chemistry and Physics*, *6*, 4705–4722.

Schotland, R. M. (1966), Some observations of the vertical profile of water vapor by a laser optical radar, in *4th Symposium on Remote Sensing of Environment*, pp. 273–283, University of Michigan, Ann Arbor.

Sherwood, T. (2005), High Availability Unmanned Aerial Platform for Carbon Cycle Measurements.

Shumate, M. S., R. T. Menzies, W. B. Grant, and D. S. McDougal (1981), Laser absorption spectrometer: remote measurement of tropospheric ozone, *Applied Optics*, *20*, 545.

Smith, K. M., and D. A. Newnham (2000), Near-infrared absorption cross sections and integrated absorption intensities of molecular oxygen (O_2, O_2-O_2, and O_2-N_2), *Journal of Geophysical Research-Atmospheres*, *105*, 7383–7396, 27.

Smith, K. M., D. A. Newnham, and R. G. Williams (2001), Collision-induced absorption of solar radiation in the atmosphere by molecular oxygen at 1.27 μm: Field observations and model calculations, *Journal of Geophysical Research-Atmospheres*, *106*, 7541–7552, 38.

Smith, N. V., S. S. Saatchi, and J. T. Randerson (2004), Trends in high northern latitude soil freeze and thaw cycles from 1988 to 2002, *Journal of Geophysical Research*, *109*(D12101).

Soloviev, A., M. Donelan, H. Graber, B. Haus, and P. Schlussel (2007), An approach to estimation of near-surface turbulence and CO_2 transfer velocity from remote sensing data, *Journal of Marine Systems*, *66*, 182–194.

Stephens, B. B., et al. (2007), Weak Northern and strong Tropical land carbon uptake from vertical profiles of atmospheric CO_2, *Science*, *316*, 1732.

Sugimoto, N., and A. Minato (1993), Long-path absorption measurement of CO_2 with a Raman-shifted tunable dye-laser, *Applied Optics*, *32*, 6827–6833.

Takahashi, T. (1961), Carbon dioxide in atmosphere and in atlantic ocean water, *Journal of Geophysical Research*, *66*, 477, 20.

Takahashi, T., et al. (2002), Global sea-air CO_2 flux based on climatological surface ocean pCO_2, and seasonal biological and temperature effects, *Deep-Sea Research Part Ii-Topical Studies in Oceanography*, *49*, 1601–1622, 48.

Tans, P. P. (2007a), NOAA Carbon Cycle Greenhouse Gases Group (CCGG): Aircraft Sampling, available online at www.cmdl.noaa.gov/gmd/ccgg/aircraft.html, accessed on November 27, 2007.

Tans, P. P. (2007b), NOAA, ESRL Online Database [www.cmdl.noaa.gov/gmd/ccgg/trends], accessed on November 27, 2007.

Tans, P. P., I. Y. Fung, and T. Takahashi (1990), Observational Constraints on the Global Atmospheric CO_2 Budget, *Science*, *247*, 1431–1438.

Tans, P. P., J. A. Berry, and R. F. Keeling (1993), Oceanic $^{13}C/^{12}C$ observations - A new window on ocean CO_2 uptake, *Global Biogeochemical Cycles*, *7*, 353–368, 35.

Turnbull, J. C., J. B. Miller, S. J. Lehman, P. P. Tans, R. J. Sparks, and J. Southon (2006), Comparison of ($^{14}CO_2$, CO, and SF6 as tracers for recently added fossil fuel CO_2 in the atmosphere and implications for biological CO_2 exchange, *Geophysical Research Letters*, *33*, 5.

Wallace, L., and W. Livingston (1990), Spectroscopic observations of atmospheric trace gases over Kitt Peak: 1. carbon-dioxide and methane from 1979 to 1985, *Journal of Geophysical Research-Atmospheres*, *95*, 9823–9827.

Wanninkhof, R. (1992), Relationship between wind-speed and gas-exchange over the ocean, *Journal of Geophysical Research-Oceans*, *97*, 7373–7382.

Wanninkhof, R., and W. McGillis (1999), A cubic relationship between air-sea CO_2 exchange and wind speed, *Geophysical Research Letters*, *26*, 1889–1892.

Wara, M. (2007), Is the global carbon market working?, *Nature*, *445*, 595–596.

Warneke, T., Z. Yang, S. Olsen, S. Korner, J. Notholt, G. C. Toon, V. Velazco, A. Schulz, and O. Schrems (2005), Seasonal and latitudinal variations of column averaged volume-mixing ratios of atmospheric CO_2, *Geophysical Research Letters*, *32*(L03808), 4, doi:10.1029/2004GL021597.

Washenfelder, R. A., G. C. Toon, J. F. Blavier, Z. Yang, N. T. Allen, P. O. Wennberg, S. A. Vay, D. M. Matross, and B. C. Daube (2006), Carbon dioxide column abundances at the Wisconsin Tall Tower site, *Journal of Geophysical Research-Atmospheres*, *111*(D22305), doi: 10.1029/2006JD007154.

Watai, T., T. Machida, N. Ishizaki, and G. Inoue (2006), A lightweight observation system for atmospheric carbon dioxide concentration using a small unmanned aerial vehicle, *Journal of Atmospheric and Oceanic Technology*, *23*, 700–710.

Webster, P. J., G. J. Holland, J. A. Curry, and H. R. Chang (2005), Changes in tropical cyclone number, duration, and intensity in a warming environment, *Science*, *309*, 1844–1846.

Yamamoto, G., and D. Q. Wark (1961), Discussion of Letter by Hanel,RA - Determination of Cloud Altitude from a Satellite, *Journal of Geophysical Research*, *66*, 3596.

Yang, S. F., M. R. Canagaratna, S. K. Witonsky, S. L. Coy, J. I. Steinfeld, R. W. Field, and A. A. Kachanov (2000), Intensity measurements and collision-broadening coefficients for the oxygen A band measured by intracavity laser absorption spectroscopy, *Journal of Molecular Spectroscopy*, *201*, 188–197.

Yang, Z. H., G. C. Toon, J. S. Margolis, and P. O. Wennberg (2002), Atmospheric CO_2 retrieved

from ground-based near IR solar spectra, *Geophysical Research Letters, 29*(9), doi:10.1029/2001GL014537.

Zimmermann, P. H., C. A. M. Brenninkmeijer, F. Slemr, A. Zahn, H. Thiemann, and H. Luthardt (2002), The CARIBIC Database: A Comprehensive Collection of Aircraft-based Measurements of Atmospheric Trace Constituents Recommended for Chemical Tracer Model Evaluation and Comparison, in *EUROTRAC-2 Symposium*.